Winter 12-15-2016

Fluorescence Imaging of Cortical Calcium Dynamics: A Tool for Visualizing Mouse Brain Functions, Connections, and Networks

Patrick William Wright
Washington University in St. Louis

WASHINGTON UNIVERSITY IN ST. LOUIS

School of Engineering and Applied Sciences
Department of Biomedical Engineering

Dissertation Examination Committee:
Beau Ances, Co-Chair
Joseph Culver, Co-Chair
Mark Anastasio
Timothy Holy
Jin-Moo Lee
Lihong Wang

Fluorescence Imaging of Cortical Calcium Dynamics: A Tool for Visualizing Mouse Brain Functions, Connections, and Networks

by

Patrick William Wright

A dissertation presented to
The Graduate School
of Washington University in
partial fulfillment of the
requirements for the degree
of Doctor of Philosophy

December 2016
St. Louis, Missouri

Table of Contents

List of Figures

List of Tables

Acknowledgements

I have been fortunate in that my years of graduate school were absolutely a positive experience in my left. Not just a net positive here at the end, not a fleeting enjoyment that would come and go—it actually spanned my entire time here. I have regularly caught myself thinking and being actively aware of the fact idea that “this is exactly what I want to be doing right now”. It would be my response to people who asked, years into the program, if I regret my choice to go to graduate school, instead of say, entering the workforce right away. “This is exactly what I want to be doing right now” would always be my response, and it was never said in attempt to convince myself that is actually how I felt, as if I were attempting to suppress feelings of listlessness or disdain. That feeling of contentment has never gone away and has been a ground truth. Looking back, I realize that was largely enabled by the environment I worked in and the people contained within. This could have easily gone south in one way or another, and that absolute truth would possibly have no longer held true. The people are what kept it constant.

First, that means thanking my advisors, Joe Culver and Beau Ances. The dual-lab setup was challenging, and had its hits and misses, but I would choose to do it again if for whatever weird, time-travely reason I am having to start graduate school over again. Both were a fantastic support system and both provided complementary advice and criticisms. I occasionally struggled to juggle both labs and sometimes felt as if I were spread thin, but especially given how accommodating both Joe and Beau were, I would not have had it any other way.

I have to thank my parents and my brother. Not only for supporting my initial plans to pursue a graduate degree, but especially for what they have done in the years since. There have been times here that I was either feeling overwhelmed or frustrated and they were always there to listen to me rant or offload.

I also have to thank my office mates. I realize that productivity of those in my immediate vicinity may wane occasionally during the workday, but that is exactly why I am grateful. Being surrounded by people who could tolerate my random questions and my spontaneous vocalized musings and observations on the most mundane topics. But that constant availability of others to bounce ideas off of while also wallowing in stupid jokes provided a baseline daily levity throughout the years.

Finally, these years would have been far less memorable if it were not for my peers and friends that I have spent time with during graduate school. The day trips, weekend trips, music festival trips, conferences, ITAP “meetings” at 2:00pm during the week (sorry Joe and Beau), the lunches, the jogs in the park, the excessive amount of time spent on Manchester, all of it. All of this is exactly what I wanted to be doing.

Patrick Wright

Washington University in St. Louis

December 2016

To my parents

ABSTRACT OF THE DISSERTATION

Fluorescence Imaging of Cortical Calcium Dynamics: A Tool for Visualizing Mouse Brain Functions, Connections, and Networks

by

Patrick William Wright

Doctor of Philosophy in Biomedical Engineering

Washington University in St. Louis, 2016

Professors Joseph Culver, Ph.D & Beau Ances, MD, Ph.D, Co-Chairs

Hemodynamic-based markers of cortical activity (e.g. functional magnetic resonance imaging (fMRI) and optical intrinsic signal imaging) are an indirect and relatively slow report of neural activity driven by electrical and metabolic activity through neurovascular coupling, which presents significant limiting factors in deducing underlying brain network dynamics. As application of resting state functional connectivity (FC) measures is extended further into topics such as brain development, aging, and disease, the importance of understanding the fundamental basis for FC will grow.

In this dissertation, we extend functional analysis from hemodynamic- to calcium-based imaging. Transgenic mice expressing a fluorescent calcium indicator (GCaMP6) driven by the Thy1 promoter in glutamatergic neurons were imaged transcranially in both anesthetized (using ketaminze/xylazine) and awake states. Sequential LED illumination (λ=470, 530, 590, 625nm) enabled concurrent imaging of both GCaMP6 fluorescence emission (corrected for hemoglobin absorption) and hemodynamics. EEG measurements of the global cortical field potential were also simultaneously acquired. First, we validated the ability of our system to capture GCaMP6

fluorescence emission and hemodynamics by implementing an electrical somatosensory stimulation paradigm. The neural origins of the GCaMP6 fluorescent signal were further confirmed by histology and by comparing the spectral content of imaged GCaMP6 activity to concurrently-acquired EEG. We then constructed seed-based FC and coherence network maps for low (0.009-0.08Hz) and high, delta-band (0.4-4.0Hz) frequency bands using GCaMP6 and hemodynamic contrasts. Homotopic GCaMP6 FC maps using delta-band data in the anesthetized states show a striking correlated and anti-correlated structure along the anterior to posterior axis. We next used whole-brain delay analysis to characterize this correlative feature. This structure is potentially explained by the observed propagation of delta-band activity from frontal somatomotor regions to visuoparietal areas, likely corresponding to propagating delta waves associated with slow wave sleep. During wakefulness, this spatio-temporal structure is largely absent, and a more complex and detailed FC structure is observed.

Collectively, functional neuroimaging of calcium dynamics in mice provides evidence that spatiotemporal coherence in cortical activity is not exclusive to hemodynamics and exists over a larger range of frequencies than hemoglobin-based contrasts. Concurrent calcium and hemodynamic imaging enables direct temporal and functional comparison of spontaneous calcium and hemoglobin activity, effectively spanning neurovascular coupling and functional hyperemia. The combined calcium/hemoglobin imaging technique described here will enable the dissociation of changes in ionic and hemodynamic functional structure and provide a framework for subsequent studies of sleep disorders and neurological disease.

Chapter 1: Introduction

1.1. Overview

Functional magnetic resonance imaging (fMRI) has been instrumental in unlocking the functional architecture of the brain and is used routinely to map the patterns of resting-state functional connectivity (RSFC) brain networks in humans [1]. However, compared to neural activity, hemodynamic measures of brain activity are relatively indirect and slow (<0.5 Hz), as they are a direct result of an intricate series of events initiated by synaptic activity, known as neurovascular coupling (NVC). Recently developed optical approaches for mapping RSFC in anesthetized mice, including optical intrinsic signal imaging (fcOIS), also have similar limitations [1, 2]. The fcOIS technique relies on differential changes in hemoglobin concentration in a manner analogous to blood-oxygen-level (BOLD) fcMRI. Similar to human fcMRI, mouse fcOIS provides a sensitive assay for several neurological diseases, including ischemic stroke [3] and Alzheimer's disease [4, 5] using functional connectivity. However, the extent of temporal and spatial information to be learned from this hemodynamic-based signal is limited. Compared to neural activity, hemodynamic measures of brain activity are relatively indirect and slow (<0.5 Hz). At infraslow frequencies (<0.1 Hz), hemodynamic signals are a reasonable report of neural activity [6-10]. Conversely, at higher frequencies, the utility of hemoglobin as a marker of neural activity is reduced. As FC becomes increasingly implemented as a tool to study brain development and disease, the need for faster and more direct neuroimaging contrasts will grow.

1.2. Neurovascular Coupling

Neurovascular coupling (NVC) is the process relating synaptic transmission and neural activity at the synapse to the downstream changes in cerebral blood flow and hemoglobin concentration [11]. The cerebral circulatory system must maintain a constant blood flow for the brain to function and accommodate regional energy utilization in the brain. The maintenance of this blood flow is maintained by the interplay of an autoregulatory component, which ensures that the brain is sufficiently supplied with blood even in the presence of sudden changes in arterial pressure, and functional hyperaemia, which is the activity-dependent increase in blood flow to regions with active neurons and astrocytes. For example, at glutamatergic synapses, following glutamate activation at the postsynapse, neurons release nitric oxide and neighboring astrocytes release arachidonic acid derivatives that act to either dilate or constrict neighboring vessels. Specifically, smooth muscle cells on neighboring arterioles and pericytes of adjacent capillaries can be contracted following neural activity, increasing vessel diameter and subsequently, blood flow to the area. The intermediate steps between synaptic activity involving transmembrane potential changes and these final changes in blood flow include an initial influx of calcium (and thus an increase in intracellular calcium concentrations), which in turn drives aerobic energy metabolism within mitochondria [11]. This full process is represented graphically in Fig. 1.1.

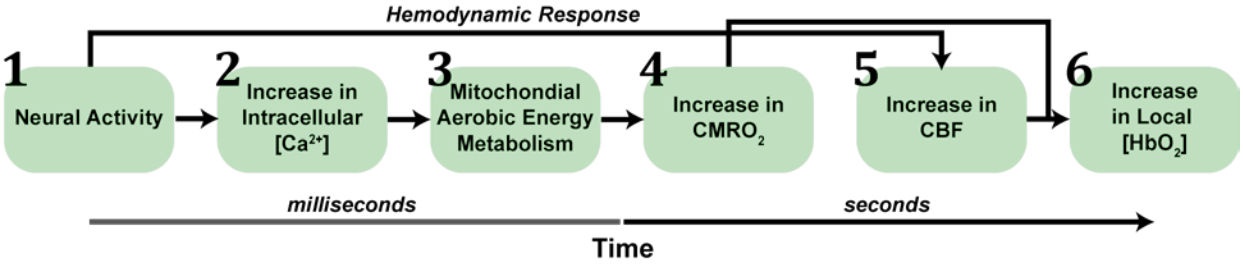

Fig 1.1. Neurovascular coupling. Cellular and hemodynamic responses to neural activity. Following an action potential, there is an increase in aerobic energy metabolism. Due to this

increased oxygen consumption, local blood flow and volume changes allow for higher HbO_2 availability. CBF: Cerebral Blood Flow. $CMRO_2$: Cerebral Metabolic Rate of Oxygen.

1.3 Functional Connectivity

Functional neuroimaging modalities have been increasingly used to elucidate the underlying functional connections of the brain. In humans, functional neuroimaging has largely been confined to imaging hemodynamic-based signals. This is largely due to the inherent methodological issues and invasiveness necessary to image fluorescent or radionuclide signals *in vivo*. Signals modulated by blood flow are endogenous and through NVC, a sufficient proxy for neural activity. One of the most promising observed phenomena using human hemodynamic imaging is the occurrence of synchronous oscillations of activity in cortical regions that are present in the absence of functional task activations, known as functional connectivity (FC). The high correspondence between the functional network topography in the correlative structure of these oscillations and functional areas revealed through functional task mapping validate the sensitivity of FC to the underlying structure of the brain. This is especially useful as a mapping method in patient populations that are unable to carry out these functional tasks.

1.3.1 Functional Connectivity Using fMRI

Currently, in humans, functional MRI (fMRI) has been used to reveal the presence of functional connections across brain networks rooted in low frequency (0.008-0.09Hz) oscillations that are correlated (and anticorrelated) in time [12]. The blood oxygen level dependent (BOLD) signal used in fMRI to observe these oscillations is based on heterogeneities of the MR signal due to the paramagnetism of hemoglobin not bound to oxygen (deoxyhemoglobin). The local concentrations

of deoxyhemoglobin decrease with neural activity, providing measurable changes in the homogeneity in the MR signal [13, 14].

1.3.2 Functional Connectivity Using Optical Modalities

These signals have also been probed optically using functional near infrared spectroscopy (fNIRS) and diffuse optical tomography (DOT) [15-17]. Compared to MRI scanners, DOT systems have the advantage of being portable, less expensive, and able to accommodate patient populations that are unable to be scanned using MRI (e.g. patients contra-indicated for MRI by having pacemakers). DOT has already been used to show FC structure in neonates and Parkinson's patients with deep brain stimulation implants [18, 19]. Intrinsic signal imaging can be implemented by using shorter wavelengths (<750nm) that fall within the visible portion of the electromagnetic spectrum. The absorption by hemoglobin of incident light at these wavelengths is orders of magnitudes higher than NIR (Fig. 1.2). Intrinsic signal imaging has been implemented in the context of FC mapping in mice and other animal models. Changes in reflectance of incident light at various wavelengths due to absorption by hemoglobin are measured and can be converted to changes in concentrations of oxyhemoglobin and deoxyhemoglobin [20]. Transcranial optical imaging of the optical intrinsic signal (OIS) has already been used to reveal these resting state functional connectivity (FC) networks in a mouse model [2]. Comparably, laser speckle contrast imaging, which measures cerebral blood flow instead of differential hemoglobin concentration changes, has been used to construct resting-state functional connectivity maps as well [21]. Optical imaging in animal models unlocks the potential to target other signals in the NVC stream that are provide complementary information to hemodynamics and are coupled to neural activity. A number of these approaches will be highlighted in the following sections.

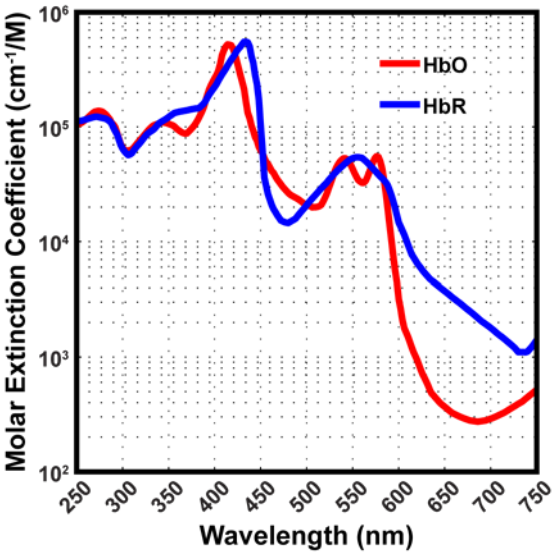

Figure 1.2. Extinction coefficient spectra of hemoglobin. Extinction coefficient spectra for oxyhemoglobin (red) and deoxyhemoglobin (blue) per wavelength. Reflectance measurements acquired using wavelengths that span these spectra can be used together to determine differential concentration changes of hemoglobin.

1.4 Functional Optical Neuroimaging

1.4.1Voltage Sensitive Dyes and Glutamate Sensors

Fluorescent voltage-sensitive dyes (VSDs) serve as sensors for transmembrane potential changes, enabling visualization of electrophysiological activity that is most commonly monitored and recorded using electrode-based modalities [22]. These probes are directly coupled to synaptic activity, enabling a temporal (μs) and spatial (50μm) specificity not possible using hemodynamic-based signals. Importantly, VSDs enable detection of subthreshold synaptic potentials. Characterizing the patterns of subthreshold inputs is necessary to understand higher brain functions such as perception. Moreover, VSD signal *in vivo* predominately originates from dendrites rather than neuronal soma due to the order of magnitude larger surface area of dendrites [23]. These have

been used to establish the seeming dependence of spontaneous cortical activity on intracortical monosynaptic structural connections [24]. Historically, a significant weakness in the use of VSDs is the invasiveness and challenge associated with cortical dye injections. More recently, genetically-encoded voltage indicators (GEVI) have been prototyped and show comparable performance to traditional VSDs, overcoming these challenges [25].

More recently, glutamate-sensing fluorescent reporters, such as iGluSnFR, have been used to visualize extracellular glutamate dynamics in awake and anesthetized mice [26]. Glutamate, as the primary excitatory neurotransmitter in the central nervous system, is implicated in learning, plasticity, general synaptic transmission and is often affected in disease. iGluSnFR has been used to visualize extracellular glutamate dynamics in the striatum in a mouse model of Huntington's disease (HD) [27]. Using this glutamate sensor, the results of this study counter a long-held mechanism underlying HD pathology: compromised glutamate uptake impairment. Rather than relying on traditional in situ synaptosomes which have been used to characterize HD previously, the observed *in vivo* results from iGluSnFR showed glutamate uptake in the HD group that were in parity with control mice. Fluorescent neurotransmitter-based probes such as iGluSnFR provide insight into

1.4.2 FAD and NADH Autofluorescence

At the most macroscopic level, the vascular response to neural activity represents the most commonly studied index of neurophysiological activity. However, this is an indirect measure of neuronal activity with a spatial distribution constrained to cerebral vasculature [28]. The inherent flexibility of optical imaging modalities allows the study of non-neurovascular signals, such as metabolic and ionic activity using autofluorescence and exogenous indicators. As a result of neuronal action potentials, there is a rapid influx of calcium into the cell which is absorbed, in part,

by mitochondria. The increased concentration of intracellular calcium following action potentials can serve as a target for imaging. This increased availability of calcium allows for aerobic energy metabolism to occur, leading to the oxidation of flavoproteins and consequently, the potential for autofluorescence. Flavin adenine dinucleotide (FAD) is an autofluorescing metabolite involved in cellular aerobic metabolism within mitochondria. FAD, derived from riboflavin, is reduced to FADH2 during the oxidation of succinate to fumarate in the tricarboxylic acid (TCA) cycle. FADH2 then acts as an electron donor in the electron transport chain of oxidative phosphorylation for the production of adenosine triphosphate (ATP). It donates each hydrogen electron in a two-step process before returning to its oxidized, fluorescing form, FAD [29-32]. Thus, variations in this fluorescence are representative of changes in mitochondrial TCA cycle rate [33] rather than changes in local hemoglobin availability.

FAD autofluorescence imaging (FAI) has been previously used to image cortical activity in vitro in cerebral slices as well as *in vivo* in both rodents and primates [33-44]. Some of these studies have highlighted the differences between metabolic signals and those hemodynamic in origin. In a study examining experience-dependent plasticity in the mouse visual cortex, FAD autofluorescence showed a faster onset time and time to peak amplitude response to visual stimulation compared to the intrinsic signal while also providing a response an order of magnitude larger [37]. Sirotin and Das showed comparable response behavior between FAI and OIS in alert macaques in response to visual stimuli. They also showed that FAI provided a more focal response early in activation with smaller point spread functions than concurrently acquired OIS [41]. Similarly, Weber and colleagues showed a faster and more localized response to single vibrissa stimulation in rats using FAI compared to cerebral blood flow (CBF) changes measured using laser speckle imaging (LSI) [36]. FAD autofluorescence changes have also been used as a marker of

mitochondrial cerebral metabolic rate of oxygen ($CMRO_2$) and compared OIS in a forelimb stimulation paradigm in rats. The FAD signal provided an evoked response with a time constant of approximately 1 second compared to the OIS time constant of 10 seconds [33]. Nicotinamide dinucleotide (NADH), which acts as an electron donor in aerobic respiration, is another autofluorescent metabolite that is fluorescent when reduced and not oxidized, in contrast to FAD autofluorescence. It has excitation and emission maxima at 350nm and 460nm, respectively, whereas FAD is maximally excited at 450nm and emits 535nm. If imaged concurrently, the ratio of FAD to NADH fluorescence ("redox ratio") provides relative changes in the oxidation-reduction state in the cell [45]. This powerful tool is often applied to tumor imaging given the abnormal redox state of tumors compared to the surrounding tissue [46].

1.4.3 Calcium Indicators

With the advent of genetic engineering techniques in mice, there are new opportunities for extending wide-field optical imaging to calcium dynamics and offer a more direct and faster measure of neural activity. Specifically, calcium concentration changes due to voltage-gated calcium channels at both the pre- and postsynapse can be imaged and visualized using fluorescent, genetically encoded calcium indicators (GECIs) [47]. These fluorophores, including GCaMP [48], are generated from modified green fluorescent protein that is coupled with a calcium binding domain, enabling increased fluorescence in the presence of elevated calcium levels and have been used extensively to study *in vivo* neural activity in C. elegans [48], mice [7, 48-52], rats [53], monkeys [54], and other animal models. Additionally, GECI expression can be driven by targeted, cell-specific (e.g. neurons or astrocytes) promotors that allow for imaging select subpopulations of cells, providing a powerful tool to map the structural and functional circuitry of the brain.

The GCaMP family consists of a circularly permuted green fluorescent protein (cpGFP), an M13 peptide, and calmodulin (CaM) which serves as the calcium binding domain. CaM and M13 interact and undergo conformational changes in the presence of calcium that cause increased fluorescence emission. Newer variants (e.g. GCaMP6) have reduced baseline fluorescence and faster kinetics than earlier generations (e.g. GCaMP3). In cultured dissociated rat hippocampal neurons, GCaMP6f has a rise time to peak following 1 to 100 action potential stimuli (driven by electrodes) of approximately 0.05-0.2s. The half decay time following 1 to 100 action potential stimuli spans 0.3-0.7s. GCaMP3, an older generation variant, has a time to peak of around 0.2s and an approximately 5-fold lower SNR than GCaMP6f. Among the GCaMP6 variant, there are three subvariants: GCaMP6s, 6m, and 6f, for slow, medium, and fast kinetics respectively. Generally, the sensors with the slowest kinetics (e.g. GCaMP6s) have the highest SNR. Regardless, the GCaMP6 sensor is sensitive to individual action potentials and is a powerful proxy for intracellular cytoplasmic free calcium [55]. It is the primary optical probe used in this dissertation.

1.5 Applications of Functional Optical Probes

1.5.1 Disease

Hemodynamic signals are based on the neurovascular coupling between increased neuronal activity and the corresponding increase in blood flow due to growing demand for oxygen and glucose [56]. In disease, this relationship has been shown to be altered in certain neuropathologies such as type 2 diabetes mellitus, Alzheimer's disease, and stroke [57-59]. This presents an application for optical probes coupled to a signal independent of NVC. In a rat model of cerebral ischemia, Baker and colleagues showed that hemodynamic (blood flow, oxyhemoglobin, and

deoxyhemoglobin) responses were more attenuated than metabolic responses with increasing ischemia severity [44]. Zhao et al showed vasoconstriction in tissue surrounding a seizure focus before ictal onset, while no changes in metabolism (measured by FAI) were observed. Moreover, hypermetabolism was observed in the focus of the seizures, supporting the increased sensitivity and possibility for FAI to create focal maps of seizure activity than those allowable by intrinsic signal imaging [42].

1.5.2 Sleep and Anesthesia

With respect to functional connectivity, GCaMP and other GECIs and VSDs offer the opportunity to map spontaneous network activity at frequencies >0.5 Hz. Furthermore, by opening up access to higher frequencies, these reporters provide a mechanism to observe and study the state of the brain during sleep, induced by either natural sleep or anesthesia, wherein the delta-band slow oscillation(0.5-4.0Hz) activity is dramatically increased[60]. The delta-band slow wave sleep phenomenon, most often observed and reported using electrophysiological techniques [61-63], consists of synchronous, oscillating alternations between depolarized and hyperpolarized neuronal states. As these waves of delta-band activity propagate over the cortex, they may interact with underlying spontaneous activity stereotypical of FC structure. For example, Lewis and colleagues have reported a fragmentation of electrophysiological FC in humans following propofol-induced loss of consciousness associated with a subsequent increase in ~1Hz cortical activity [64].

Sleep can be delineated into periods of rapid eye movement (REM) sleep, in which there are rapid, binocularly symmetrical eye movements, and non-REM (NREM) sleep which is characterized by a distinctive EEG pattern of “sleep spindles” occurring at ~12-14Hz and high amplitude, slow “delta” waves. NREM sleep consists of 3 stages, with so-called “slow wave sleep” occurring

during stage 3 [65]. During light periods, mice spend approximately 25-50% of their time awake, 50-70% in NREM, with the remaining ~5% time spent in REM. Because mice are nocturnal, during dark periods, time in wakefulness is maximized (>75%), with time in NREM making up ~20% of the total dark time and REM the remaining ~2% [66]. The primary cellular component underlying NREM sleep is a slow oscillation (0.5-2.0Hz) of the membrane potential of cortical neurons. Using a 256-channel high-density EEG system in humans (n=8), Massimini and colleagues show that each cycle of this slow oscillation is a traveling wave that originates in prefrontal-orbitofrontal regions and propagates along the anterior-posterior axis, sweeping the cortex [67]. This phenomenon was stable and reproducible within and across subjects and across nights. This neuronal oscillation consists of alternation between periods of membrane potential hyperpolarization ("down states", a period of neuronal silence) and depolarizing envelopes ("up states"), first described by Steriade and colleagues in cats using intracellular recordings [61]. In natural sleep, these oscillations occur at approximately 0.4Hz, but can be pharmacologically modulated. For example, in the presence of ketamine/xylainze, the duration of the depolarizing "up" envelope was reduced, increasing the overall frequency of oscillation to ~1Hz.

In the context of resting-state activity, using BOLD fMRI, Mitra and colleagues established the delay topography in normal adults during wakefulness and slow wave sleep [68]. They demonstrated that subcortical structures are early in relation to the cortex during wakefulness, but are late during slow wave sleep. They also observed that across resting-state networks, propagation was significantly altered in slow wave sleep compared to wakefulness, but within resting-state network propagation was preserved.

Nevertheless, the extent that delta-band activity influences functional network structure is unknown. The ability of these fast optical probes, specifically GCaMP6, to be used as an FC

mapping tool and the state-dependence of calcium-based FC structure must be characterized. Because hemodynamic-based measures cannot be used to directly probe this activity, GCaMP6 provides a unique approach for examining these oscillations and their relation to spontaneous FC structures.

In this dissertation, we report concurrent imaging of hemoglobin and GCaMP6 dynamics in a Thy1/GCaMP6 transgenic mouse model [52]. An optical imaging system and algorithms were developed to image wide-field calcium and hemoglobin dynamics concurrently over three decades of frequency (0.008Hz to 8 Hz). We first quantified the duration of spontaneous GCaMP6 data necessary to construct canonical FC images. The patterns of FC within the infraslow (0.008-0.09Hz) spontaneous GCaMP6 and HbO_2 dynamics were then explored using canonical seed-based intercontrast FC analysis. Since GCaMP6 enables analysis at higher frequencies, we characterized delta-band (0.4-4.0Hz) GCaMP6 activity across the cortex in both anesthetized and awake states, to evaluate the possibility of a state-dependence of calcium-based FC topography. Spectral features of GCaMP6 dynamics were compared to simultaneously-measured EEG to validate the sensitivity of GCaMP6 to global cortical electrophysiological activity and to state (awake or anesthetized). Finally, cortical propagation in GCaMP6 was examined during the transition from anesthetized state to wakefulness. The technology developed here for concurrent GCaMP6/hemodynamic imaging will provide a framework both for mapping calcium- and hemoglobin-based FC and for understanding how neurovascular coupling is altered in disease.

Chapter 2: METHODS

2.1 GCaMP6/Thy1 Transgenic Mice

Transgenic mice expressing GCaMP6 driven by the thymus cell antigen 1 (Thy1) promotor were acquired from Jackson Laboratories (JAX Strain: C57BL/6J-*Tg (Thy1-GCaMP6f)GP5.5Dkim*; stock: 024276)[52, 55]. In this model, GCaMP6 expression is widespread in the CNS (e.g. cortex, hippocampus, thalamus, and cerebellum) and localized predominantly to excitatory projection neurons [69]. GCaMP6/Thy1 transgenic genotypes were confirmed by PCR using the forward primer 5'-CATCAGTGCAGCAGAGCTTC-3' and reverse primer 5'-CAGCGTATCCACATAGCGTA-3'.

2.2 Animal Preparation

All procedures have been approved by the Washington University School of Medicine Animal Studies Committee. Seven GCaMP6 mice (12-16weeks of age, 28-36g) were used in all experiments in this thesis. Mice were sedated with isoflurane (3% induction, 1% maintenance, 0.5 L/min) and placed in a stereotactic holder. The head was then shaved, and a midline incision made to expose the skull. Body temperature was maintained at 37°C using a temperature controlled heating pad. Following scalp retraction, pilot holes were drilled into but not penetrating the skull at approximately -1mm posterior to bregma, and +/- 5mm lateral to bregma (near barrel/auditory cortex). Small stainless steel self-tapping screws (BASI Inc., West Lafayette, IN, USA) were then inserted into these holes for collecting EEG recordings. Chronic cranial windows made of Plexiglas and with pre-tapped holes were fixed to the skull using dental cement (C&B-Metabond, Parkell Inc., Edgewood, NY, USA).

2.3 Epifluorescence and Confocal Imaging

Mice were deeply anesthetized with FatalPlus™ (Vortech Pharmaceuticals, Dearborn, MI, USA) and transcardially perfused with 0.01 M PBS. The brains were removed and fixed in 4% paraformaldehyde for 24 h and transferred to 30% sucrose in 0.2 M PBS. After brains were saturated, they were snap-frozen on dry ice and coronal sections, 50μm thick, were made with a sliding microtome. Sections were stored in 0.2 M PBS, 30% sucrose, and 30% ethylene glycol at −20°C. For viewing, cut sections were washed in PBS, mounted, and intrinsic GCaMP6 fluorescence was examined with epifluorescence microscopy (Nikon Eclipse 80i, Nikon Instruments Inc., Melville, NY, USA). For viewing using confocal microscopy, additional cut sections were washed in PBS, mounted, and coverslipped in DAPI containing mounting media (Vector Laboratories, Burlingame, CA, USA). Fluorescent images of DAPI labeled cells and intrinsic GCaMP6 fluorescence were then acquired with a Nikon A1-Rsi inverted confocal microscope. Excitation illumination was provided by 405nm and 488nm lasers for DAPI and GCaMP fluorescence, respectively (Nikon Eclipse 80i, Nikon Instruments Inc., Melville, NY, USA).

2.4 *In Vivo* Optical Imaging System

Sequential illumination was provided by four LEDs: 470nm (blue), 530nm (green), 590nm (yellow), and 625nm (red). The 470nm LED is used for GCaMP excitation, and the 470nm, 530nm, 590nm, and 625nm LEDs are used for hyperspectral oximetric imaging. The 530nm LED was also used as an emission reference for GCaMP6 fluorescence in order to remove any confound of hemodynamics in the fluorescence signal (described below). Both the 470nm and 530nm LED light paths were made collinear by using a multi-wavelength beam combiner dichroic mirror

(Mightex Systems, Pleasanton, CA, USA). For image detection, we used a cooled, frame-transfer EMCCD camera (iXon 897, Andor Technologies, Belfast, Northern Ireland, United Kingdom) in combination with an 85mm f/1.4 camera lens (Rokinon, New York, NY, USA). Acquisition frame rate was 16.8Hz, well above respiration rates (approximately 3 Hz) and fast enough to adequately characterize hypothesized GCaMP6 activity. Images were acquired in five minute sessions. To increase frame rate as well as increase SNR, the CCD was binned at 4 x 4 pixels; this reduced the resolution of the output images from full-frame 512 x 512 pixels to 128 x 128 pixels but allowed for increased frame rate. Both the LEDs and the exposure of the CCD were synchronized and triggered via a DAQ (PCI-6733, National Instruments, Austin, TX, USA) using MATLAB (MathWorks, Natick, MA, USA). The field-of-view was adjusted to be approximately 1 cm^2 square resulting in an area that covered the majority of the convexity of the cerebral cortex with anterior-posterior coverage from the olfactory bulb to the superior colliculus. The resulting pixels were approximately 78µm x 78µm. To minimize specular reflection from the skull, we used a series of linear polarizers in front of the LED sources and the CCD lens. The secured mouse was placed at the focal plane of the camera. The combined, collimated LED unit was placed approximately 8 cm from the mouse skull, with a working distance of approximately 14cm as determined by the acquisition lens. A 515nm longpass filter (Semrock, Rochester, NY, USA) was placed in front of the CCD to filter out 470nm fluorescence excitation light and a 460/60nm bandpass filter (Semrock, Rochester, NY, USA) was used in front of the excitation source to further minimize leakage of fluorescence excitation light through the 515nm longpass filter. The pulse durations for the LEDs are 20ms, 5ms, 3ms, 1ms for 470nm, 530nm, 590nm, and 625nm, respectively.

2.5 Electrical Hindpaw Stimulation

Electrical stimulation was generated using an isolated pulse stimulator (Model 2100, A-M Systems, Carlsborg, WA, USA) delivered to the left hindpaw of each mouse via micro vascular clips (Roboz Surgical Instrument Co., Gaithersburg, MD, USA) during the somatosensory activation imaging sessions. The stimulation block paradigm consisted of an initial rest period of 5 seconds followed by four seconds of electrical stimulation at an application frequency of 2Hz (pulse duration: 300μs, current: 0.5mA) and ending with 51 seconds of rest. This 60 second block was repeated five times during each five minute imaging session for subsequent block averaging.

2.6 Anesthetized Imaging

For anesthetic imaging, mice were anesthetized with intraperitoneal injection of a ketamine/xylazine cocktail (86.9 mg/kg Ketamine, 13.4 mg/kg Xylazine). Anesthetic effect was verified by confirming that the animal was not responsive to a hind paw pinch. The animal was placed and kept on a solid state water circulating heating pad (T/Pump Classic, Stryker Co., Kalamazoo, MI, USA), maintained at 42°C , to minimize electronic noise in the EEG signal.

2.7 Awake Imaging

We constructed a customized apparatus consisting of a felt pouch suspended by optical posts. This provided a dark, comfortable environment while preventing the awake mouse from putting torque on their restrained head. During the imaging session, the mouse was able to move freely while its head was secured. After recovery from this surgery (1 week), the mouse was then acclimated to the apparatus by a training period consisting of two 20min sessions. Acclimation is indexed by a return to normal behavior (e.g., whisking, grooming, and walking with head restrained). Once

acclimated, mice were mounted to the imaging system with a small bracket (using the window's pre-tapped holes) with the body of the mouse placed inside the felt pouch. Imaging then proceeded as described above.

2.8 EEG Recording and Processing

Summed field potentials were concurrently recorded with OIS imaging sessions from the 2 screws implanted in the skull and digitized at 1kHz (AD Instruments Power Lab EEG Amplifier). EEG frequency spectra were calculated by splitting data from each 5min session into thirty 10s epochs, applying a 10s Hann window to each, calculating the Fast Fourier Transform, then averaging the squared modulus of each epoch together.

2.9 Image Processing

A representative frame of baseline light levels in a dark environment, calculated from a mean of dark images collected over 1 minute, was subtracted from the raw data. All pixel time traces were detrended to remove any variations in light levels due to photobleaching, LED current drift, and nonuniformity across the skull [40]. Reflectance changes in the 470nm, 530nm, 590nm, and 625nm LED channels were used in combination to provide oximetric data using the Modified Beer-Lambert Law, described previously [2]. Images in each contrast were smoothed with a Gaussian filter (5x5 pixel box with a 1.3 pixel standard deviation).

The GCaMP6 fluorescent signal must be corrected for any contribution from vascular activity and varying concentrations of absorptive hemoglobin. Though the effects of hemodynamics will likely not mask the emission signals entirely, they will influence them. Common correction methods to calculate relative fluorescence changes include using a reference wavelength for applying

subtraction and ratiometric techniques. We implemented a ratiometric correction algorithm (Equation 1) to correct fluorescent emission for any absorption by hemoglobin and deoxyhemoglobin using the reflectance channels at the GCaMP6 emission wavelengths (530nm LED) as a reference.

$$Eqn.\ 1\ y(t) = \frac{I^{em}(t)}{I^{ref}(t)} \cdot \frac{I_0^{ref}}{I_0^{em}}$$

I^{em} refers to the detected fluorescent emission intensity. I^{ref} describes the measured reflectance changes at the emission wavelength. A single frame from the 628nm reflectance channel was loaded into Adobe Photoshop CC 2014 (Adobe Systems, San Jose, CA, USA) and all regions not corresponding to brain were manually painted white. The image was loaded back into MATLAB and used to create a binary brain mask. All subsequent analysis was performed on those pixels labeled as brain. Image sequences from each mouse (as well as the brain mask for each mouse) were affine-transformed to a common atlas space (based on the Paxinos mouse atlas) using the positions of bregma and lambda (Franklin & Paxinos, 2008). The time traces of all pixels defined as brain by the binary mask were averaged to create a global brain signal. This global signal was regressed from every pixel's time trace to remove global sources of variance. For all analysis involving spontaneous activity, data were filtered over either the canonical functional connectivity frequency range (0.009-0.08Hz) [1] or the delta activity band (0.4-4.0Hz). Evoked activity was lowpass filtered at 6Hz to remove high-frequency noise. This pre-processing stream is represented graphically in (Fig. 2.1).

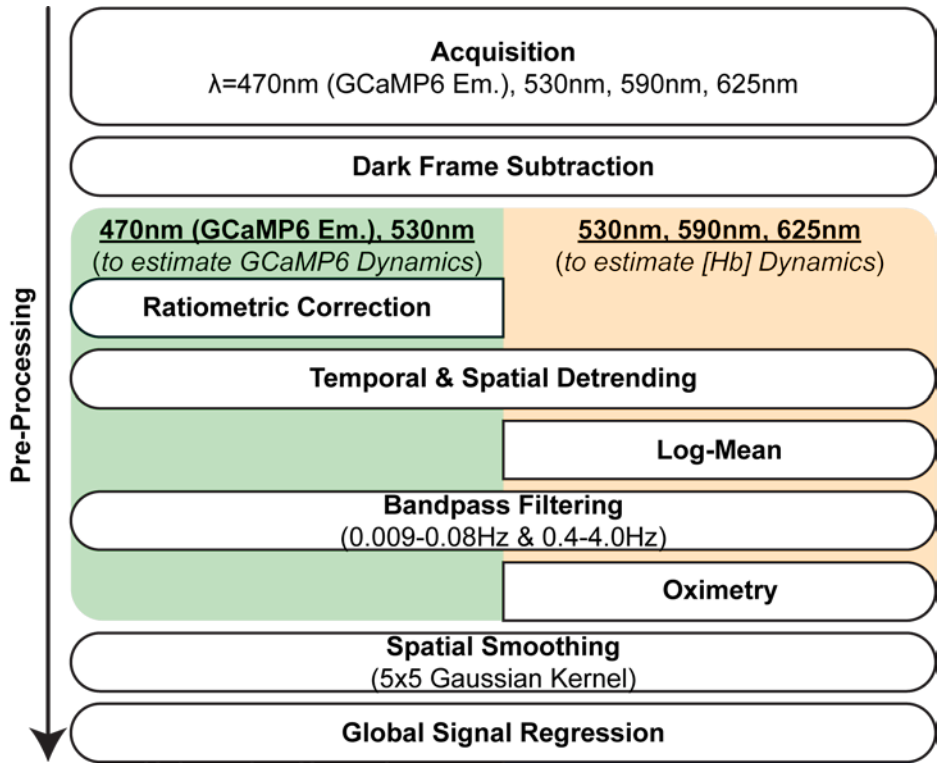

Figure 2.1. Pre-processing stream for acquired GCaMP6 and OIS image series. Pre-processing stream from acquisition of raw reflectance measurements (λ=530nm, 590nm, 625nm) used for estimating differential hemoglobin concentration changes (right half) and raw GCaMP6 fluorescence emission (used with 530nm in a ratiometric correction algorithm to remove confounding hemoglobin absorption from the fluorescent signal) through detrending, bandpass filtering, spatial smoothing, and global signal regression. Data are then prepared for use in subsequent functional connectivity, coherence, and spectral analyses.

2.10 Spectral Analysis

To construct frequency spectra of spontaneous GCaMP6 activity, time series at each pixel were split into two 150s windows (per each 5min imaging session), windowed with 150s long Hann

functions, and then the Fast Fourier Transform was calculated. The squared moduli of these FFTs were then averaged across the brain to produce the final power spectra.

2.11 Seed-Based Functional Connectivity

Using the Paxinos histological atlas as a reference, seed locations were chosen at coordinates corresponding to the left and right visual, motor, somatosensory, cingulate, parietal, auditory, and retrosplenial cortices. A 0.5 mm diameter circle at each seed location was averaged to create a seed time trace. These seed traces were correlated against every other brain pixel to create functional connectivity maps. FC maps were calculated for every 5 minute imaging session, Fisher z-transformed (using the inverse hyperbolic tangent function) to improve normality and stabilize the variance of the correlation coefficients, averaged across all imaging sessions and mice, then finally reverse transformed (using the hyperbolic tangent function) back to correlation coefficients. Matrices consisting of the correlation coefficient between each pair of network seed traces were constructed by plotting the pairwise correlation coefficients in each cell. A form of Dice's coefficient was calculated (Eqn 2) to compare spatial similarity of variable length time and sampling window FC maps and maps created using group averaged data. Dice's coefficient was calculated using:

$$Eqn.\ 2\ \ Sim = \frac{2\sum_{i=1}^{d} A_i B_i}{\sum_{i=1}^{d} A_i^2 + \sum_{i=1}^{d} B_i^2}$$

Where *s* is the spatial similarity, and *A* and *B* are the FC maps being compared.

2.12 Seed-Based Coherence

The magnitude-squared, band-averaged real and imaginary coherence (Coh) values were calculated using spontaneous GCaMP6 data from both the ketamine/xylazine-anesthetized and awake states. Coherence, ranging from 0 to 1, is analogous to correlation in the frequency domain, with the real component of coherence between two signals providing a measure of shared spectral content, independent of phase, whereas the imaginary coherence estimates of degree of shared spectral content at non-zero delays. Using pre-processed data bandpassed filtered from 0.4-4.0Hz, the coherence (Eqn. 3) was calculated between each seed trace and all pixels across the FOV.

$$Eqn.\ 3\ Coh_{xy}^{2}(\overline{k}) = \frac{\left|\sum_{k=k1}^{k2} \hat{G}_{xy}(k)\right|^{2}}{\sum_{k=k1}^{k2} \hat{G}_{xx}(k) \sum_{k=k1}^{k2} \hat{G}_{yy}(k)}$$

G_{xy} is the cross-spectra of both time series, and G_{xx} and G_{yy} are the auto-spectra of each time series.

2.13 Whole-Brain Delay Analysis

The GCaMP6 time series from every pixel was cross-correlated with the global signal (described above) to reveal any phase shifts (quantified as time lags). The temporal shift that maximizes the correlation between both time series was plotted at each pixel to create a map of delay topography across the cortex.

2.14 Parcellation

To parcellate the brain into functional regions, we implemented an iterative, data-driven approach. Using sixteen canonical bilateral seeds as the initial condition, the organization of the neuroarchitecture can be refined with a method consisting of two steps: (1) updated time traces are found for each parcel (the seeds being the starting “parcels”) by averaging over all pixels in each

parcel, (2) updated spatial arrangements are found for each parcel by calculating the correlation coefficient between the time traces for each pixel and each parcel and subsequently assigning every pixel to the parcel with which it maximally correlated. New averaged time traces are calculated for each updated parcel spatial arrangement (a return to Step 1). This process is repeated until no pixel changes region from one cycle to the next. If at any point in the iterative scheme a parcel had fewer than ten pixels (0.04 mm^2), it was eliminated from the analysis, thus preventing the development of overly small parcels (a pixel will have the highest possible correlation coefficient with a parcel consisting solely of itself).

2.15 Statistical Analysis

To compare differences in functional connectivity network maps across the anesthetized and awake states, two-tailed Welch's unequal variances t-tests were used to compare Fisher z-transformed correlation coefficients at every pixel. T-statistic maps were then created and subsequently thresholded using a Bonferroni-adjusted significance level of α=3e-6. Two-tailed paired t-tests were used to compare differences at each pixel in the visual network functional connectivity maps in the mouse transitioning from anesthesia to wakefulness. Each five minute epoch was divided into ten 30 second windows for all comparisons across epochs. Calculated t-statistic maps were thresholded using q=0.001 after false discovery rate adjustment. Two-tailed Welch's unequal variances t-tests were used to compare the full width at half maximum values for both the ipsilateral and contralateral horizontal line profiles from each seed-based functional connectivity map.

Chapter 3: RESULTS

3.1 Histology of Fixed Coronal Slices from Thy1/GCaMP6 Mice

To confirm GCaMP6 fluorescence was present in superficial cortical layers, corresponding to the maximal depth of the imaging system, paraformaldehyde-fixed GCaMP6 brain slices were imaged using both epifluorescence (Fig. 3.1A) and confocal (Fig. 3.1B) microscopy. Individual neuronal somas (Fig. 3.1B, green: GCaMP6, blue: DAPI stain) and their neurites are detectable throughout cortical layers I – VI (Fig. 3.1B) and across the cortex (Fig. 3.1A, green: GCaMP6).

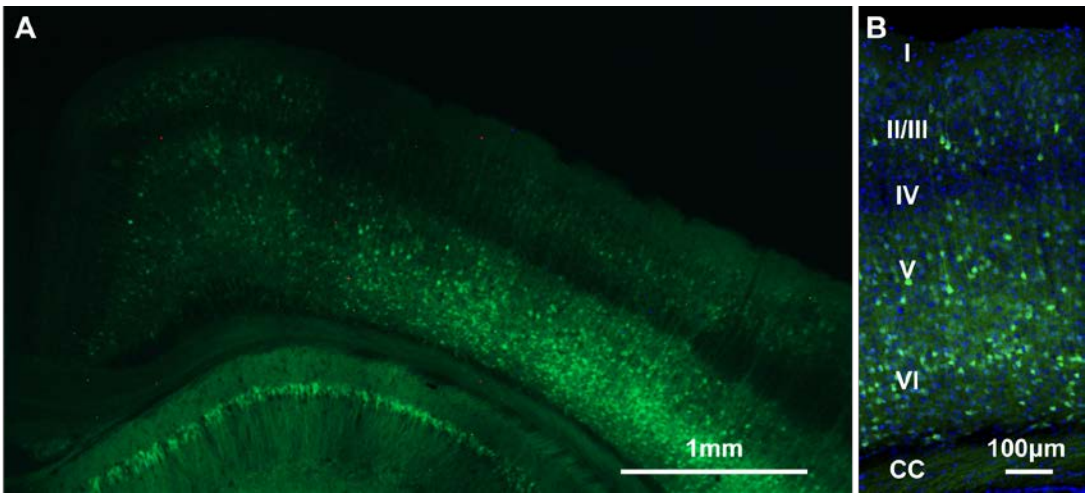

Figure 3.1. Histology of coronal slices collected from a representative Thy1/GCaMP6 mouse. Thy1/GCaMP6 Mouse Model Validation. Based on previous studies, Thy1/GCaMP6 fluorescence should provide a signal predominantly driven by cortical neuronal neurons and that is faster than hemodynamic measures A). Epifluorescence (A) and confocal (B) images of 50um coronal slices collected from a representative Thy1/GCaMP6 mice. GCaMP6 expression (green) is located throughout the cortex (i) and localized to neuronal soma (ii, blue-DAPI stain) and can be seen throughout cortical layers I-VI.

3.2 Concurrent Imaging of GCaMP6 Fluorescence and Hemodynamics

In order to enable consistent, repeatable imaging sessions while minimizing number of invasive surgical procedures, all mice had a plexiglass optical imaging window implanted. Following a one-time scalp retraction, these windows are adhered to the skull using dental cement and can stay in place for at least three months (Fig. 3.2A). During this same surgical procedure, two self-tapping bone screws were implanted bilaterally one (ground) is implanted posteriorly near the cerebellum to allow for global field potential recording during all imagining sessions (Fig. 3.2A). After window implantation, mice were mounted in a suspended felt pouch that fixes the skull at the imaging plane but does not prevent the mice from moving their limbs freely (Fig. 3.2B). This imaging state was used for all ketamine/xylazine-anesthetized and awake imaging sessions.

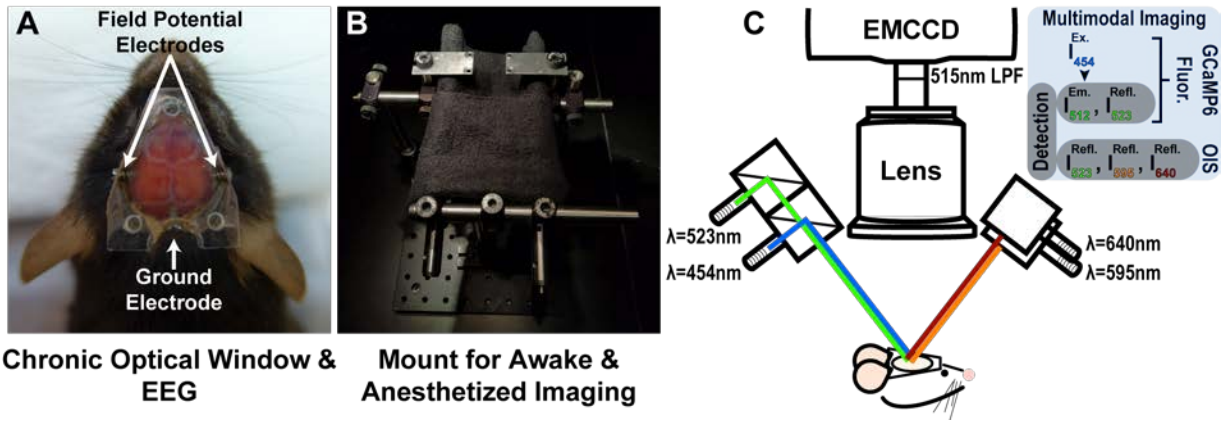

Figure 3.2. Concurrent GCaMP6 fluorescence, OIS, and EEG system for chronic imaging in awake and anesthetized mice. A) Chronic plexiglass optical window implant enables for non-invasive, consistent repeat imaging sessions. Two bilaterally-implanted electrodes are used to measure global field potential EEG during imaging. B) Felt pouch used for both awake and ketamine/xylazine-anesthetized imaging. C) Schematic of the combined GCaMP and OIS imaging

system. GCaMP excitation and reference LEDs share a collinear optical path using dichroic mirrors. Green (λ=523nm), yellow (λ=595), and red (λ=640) are used together to determine differential concentration changes of hemoglobin. Detection is done using a cooled EMCCD with an 85mm f/1.4 lens.

In order to image both GCaMP6 activity and hemodynamics concurrently, we developed an optical imaging system with multiple illumination wavelengths that were temporally multiplexed. A filtered detection scheme provided both fluorescence and reflectance imaging. To image GCaMP6 fluorescence, we selected incident LEDs wavelengths that match both the excitation (peak lambda=497nm) and emission (peak λ=512nm) spectra of GCaMP6 (Fig. 3.3A&B). The fluorescence measurement includes transport of light from the tissue surface through the brain, excitation of subsurface GCaMP6 and fluorescence emission, followed by the emitted light transporting back out of the tissue and being collected by the lens and focused onto the detector. The transport of light through the tissue will be modulated by changes in absorptive hemoglobin concentration. Thus, the dynamics of the detected GCaMP6 fluorescence emission will be a product of both the GCaMP6 dynamics and local hemodynamics [70]. To provide a strategy for correcting the raw fluorescence measurement for dynamic absorption changes, we incorporated a reference reflectance measure, specifically, reflectance from the green LED (peak λ=523nm), roughly equivalent to the GCaMP6 emission spectrum, was used as a reference measure in a ratiometric correction algorithm (see Chapter 2) to provide a signal that better tracks underlying calcium dynamics.

The green LED was also used along with yellow (peak λ=595nm) and red (peak λ=640nm) LEDs for concurrent calculation of differential changes of hemoglobin concentration (see Methods) (Fig.

3.2C). The excitation light (peak λ=454nm) was blocked between the lens and the detector using a 515nm longpass filter (Fig. 3.2C, Fig.3.3A&B). Light was detected for all wavelengths using an electron multiplying charge coupled detector (EMCCD, iXon 897, Andor Technologies). After multiplexing through all four illumination LEDs, the resulting GCaMP6 and HbO_2 frame rate was 16.8Hz.

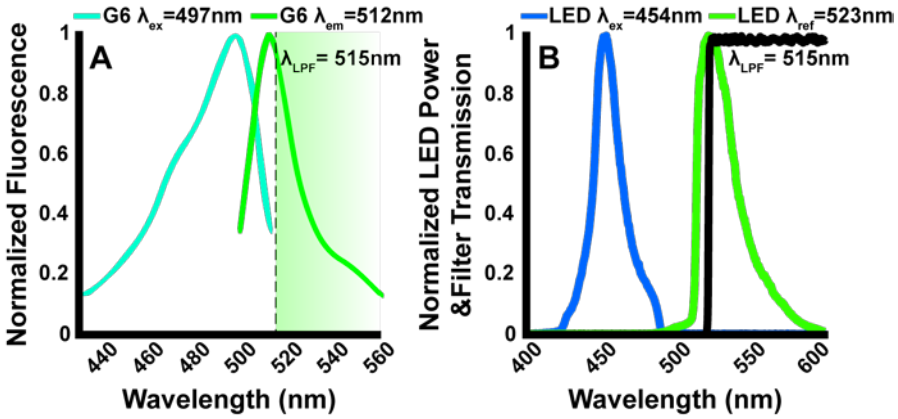

Figure 3.3. GCaMP6 fluorescence excitation and emission spectra. A) GCaMP6 dynamics are imaged using fluorescence measurements, wherein the fluorophore has a peak excitation at λ=497nm and peak emission at λ=523nm spectra for GCaMP. A longpass filter at λ=515 nm is used to block fluorescence excitation light. B) Spectra from the excitation LED (λ =454nm, bandpass filtered at 460/60 nm). A reference (λ =523nm) LED is used for correcting for changes in optical properties due to the presence of absorptive hemoglobin. The transmission curve for the 514nm longpass filter at detection is shown for reference.

3.3 GCaMP6 Fluorescence is Detectable and Temporally Distinct from HbO_2

To evaluate the mapping fidelity of both the GCaMP6 and hemoglobin contrasts and the ratiometric correction strategy, we used a block design electrical hindpaw stimulation paradigm (each block consisted of 4 seconds of stimulation at 2 Hz, followed by 51 seconds of rest; 50 blocks

across n=7 mice were included in analysis). Maps of the spatial extent of hindpaw cortex, contralateral to stimulation, for both GCaMP6 and HbO_2 show well-localized responses (Fig. 3.4A). Before ratiometric correction, each electrical pulse is present in the raw GCaMP6 signal (Fig. 3.4B, dark green). However, during the stimulus, after initially rising, the raw fluorescence signal rapidly decreases, which is due to increased absorption (Fig. 3.4B, light green) from the increased blood volume and hemoglobin concentration (Fig. 3.4, red trace). After ratiometric correction for absorption, the GCaMP6 signal increases and stays elevated until returning to baseline approximate 6 seconds post stimulus. The evoked responses corresponding to HbO_2 (Fig. 3.4B, red trace) and HbR (Fig. 3.4B, blue trace) have an onset approximately 2 seconds after the initial stimulus presentation. Also, the observed ratio of HbO_2 to HBr peak magnitudes is approximately 3:1, as expected from canonical functional responses [71]. These results suggest the correction algorithm sufficiently unmixes and estimates HbO_2 and HbR dynamics using 530nm, 590nm, and 625nm together for oximetry and collectively demonstrate the ability of the hardware and algorithms to concurrently image both calcium dynamics (via GCaMP6) and hemodynamics.

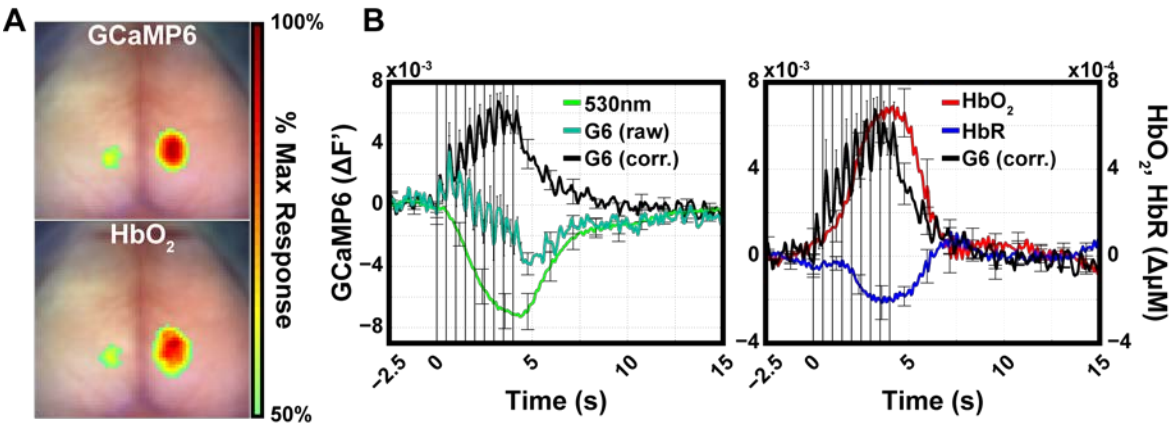

Figure 3.4. Somatosensory functional activations in concurrently-acquired GCaMP6 and OIS. A) Maps of stimulus evoked responses to electrical stimulation of left hindpaw (thresholded

at >50% peak response). B) Time series of evoked responses sampled using masks created from the right half of the 50% peak response images in part B. Green reflectance (green trace, top panel) is used to correct raw GCaMP6 emission (teal trace) for absorption due to hemodynamics using a ratiometric approach (see Chapter 2; the corrected trace is black). This corrected GCaMP6 trace (black) is sensitive to each stimulus presentation (black trace, lower panel), whereas HbO_2 (red) and HbR (blue) follow the slower, canonical hemodynamic response. Data from 50 blocks across 7 mice are included in all evoked analysis.

3.4 Functional Connectivity Mapping in GCaMP6 Mice

Functional connectivity was quantified by calculating the correlation between the time traces in two distinct brain regions (Fig. 3.5). In order to facilitate comparisons of fcMRI and the functional connectivity analysis using the concurrent GCaMP6/hemodynamic imaging system, we implemented a standard functional connectivity processing pipeline across two frequency bands: 0.009-0.08Hz ("infraslow") and 0.4-4.0Hz ("delta-band") for all contrasts. For resting-state imaging sessions during anesthesia and wakefulness, each mouse was stabilized using the chronic implanted optical window that was fixed at the imaging plane. Mice were secured in a suspended felt pouch that allowed free limb movement. After imaging and pre-processing, the whole brain global signal was regressed out from the imaging data the whole brain global signal to remove potentially confounding shared variance across the cortex [3]. Seed-based functional connectivity was then performed using spontaneous GCaMP6 and HbO_2 activity across frequencies and states. In an illustrative example for spontaneous GCaMP6 data measured in wakefulness, the time series sampled from left motor and contralateral right motor cortices (Fig. 3.5, black & red traces and circles, respectively) over the infraslow band are highly correlated (r=0.95), whereas the

correlation strength between the left motor seed and right cingulate cortices is low (r=0.08). Functional connectivity maps were constructed by calculating the position dependent correlation coefficient between this left motor seed and the time series at every pixel across the field-of-view (Fig. 3.5, top right). This same analysis was applied to the higher frequency band (Fig, 3.5, bottom), which shows conservation of the functional relationships observed in the infraslow frequencies.

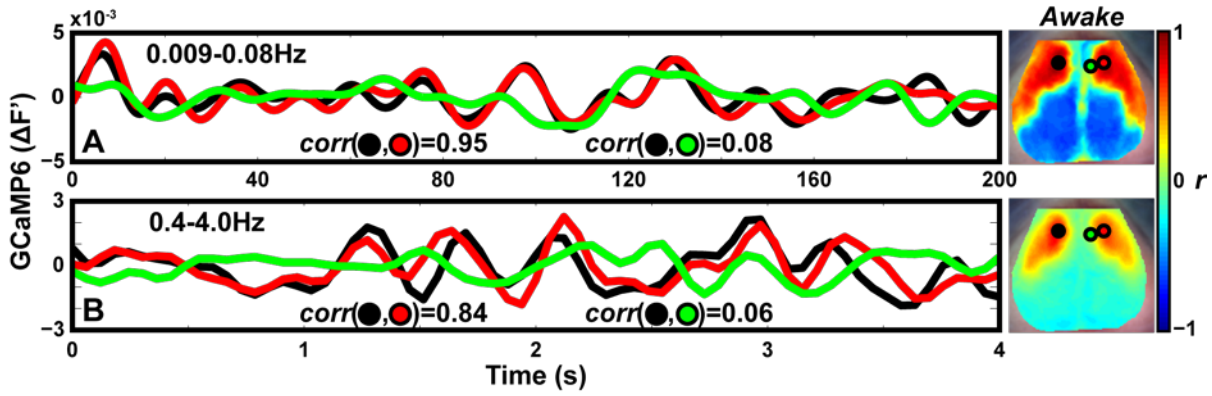

Figure 3.5. Performing functional connectivity analysis in the awake mouse brain. Time series of spontaneous GCaMP6 activity filtered over the canonical functional connectivity band: 0.009-0.08Hz (top) and the delta band: 0.4-4.0Hz (bottom). Black and red traces and seeds correspond to left and right somatosensory cortices, respectively. Green is sampled from left cingulate cortex. Over both frequency bands, left and right somatosensory cortex show highly correlated activity whereas right somatosensory with left cingulate show reduced temporal correlation. At the pixelwise level, correlating the time series from the left somatosensory (black) with every pixel in the brain produces a map showing homotopic functional somatosensory structure across hemispheres.

Because GCaMP6 is able to probe activity at frequencies higher than traditionally associated with FC (i.e. <0.1Hz), we examined the effect of time window length on the stability of the FC patterns. Using data acquired in the awake state and filtered over the delta frequency band (0.4-4.0Hz) in a spatial similarity analysis, we compared the effect of increasing time window length, ranging from 2.6 seconds to 300 seconds and sampled from a single 5 minute imaging session from one mouse (Mouse 2). For each window length, we calculated the similarity between the individual mouse FC map from each network and the respective reference template calculated from longer data acquisitions with averaging across mice (i.e. group-level) maps (Fig. 3.6A). Using only 30s of data from an individual mouse, the FC maps constructed with 7 canonical seeds have distinct qualitative network-specific structure (Fig. 3.6B). The similarity between FC maps based on 30s of data vs. the group is consistent for all 7 networks for all mice (Fig. 3.6C). To evaluate the stability of the maps over time, the FC map for a seed placed in motor cortex was constructed for a sequence of overlapping 30s segments of data, shifted by increments of 2.6 seconds, for all mice and compared to the group-averaged map. The similarity score remains relatively consistent across the entire 5 min session (Fig. 3.6D). Collectively, these data imply that windows with a duration as short as 30s can produce stable FC maps when using GCaMP6 data. The robustness of the GCaMP6 FC maps from these 30s windows is relatively independent of temporal sampling location, network seed, and mouse.

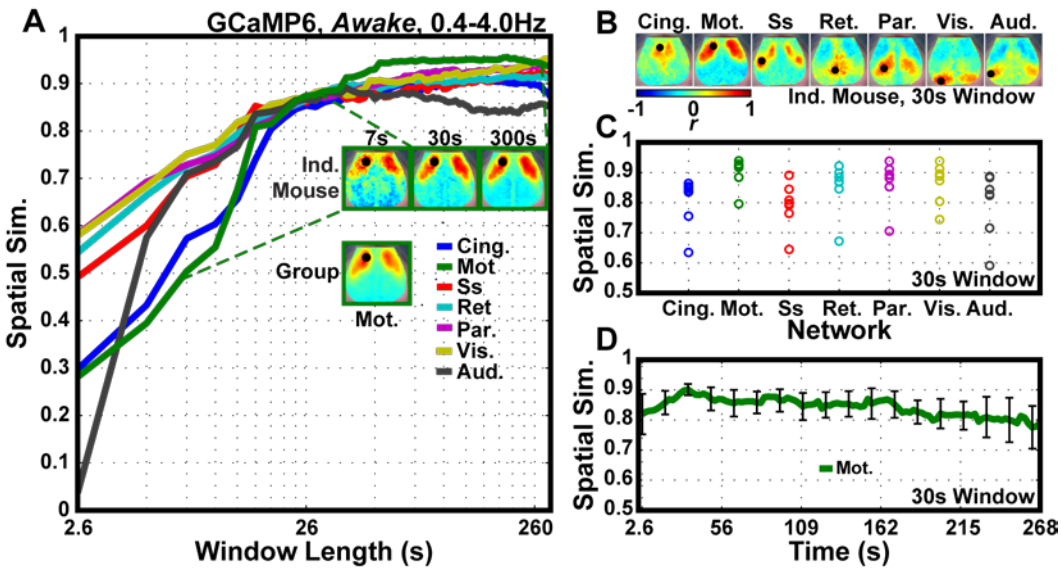

Figure 3.6. Stability and stationarity of spontaneous GCaMP6 activity in functional connectivity analysis. A) FC maps were constructed using time windows of spontaneous 0.4-4.0Hz GCaMP6 (awake) data of increasing length from one mouse (Mouse 2). Windows were increased in length by ~2.6s up to ~300s. Spatial similarity (based on Dice's coefficient) was calculated between each of these FC maps for all networks relative to their corresponding group level map. The FC maps calculated by using a seed in left motor cortex are highlighted as an example. Across all networks, similarity scores converge at 0.9 with a window length of ~30s. B) Seed-based FC maps from Mouse 2 constructed using 30s of spontaneous GCaMP6 data. C) For each of 7 networks, the same 30s window of spontaneous data for each network was compared to the corresponding group-level network FC map for all mice. The stability of similarity of 30s of data is present across network and across mice. D) Using consecutive 30s windows (sampled every ~2.6s) from a single 300s imaging session from each mouse, the spatial similarity between all 30s motor FC maps and the group level motor FC map is shown to be relatively stationary. Error bars are standard error of the mean.

3.5 Intercontrast FC Between Delay-Shifted GCaMP6 and HbO_2

To further validate the ability of the system to properly unmix HbO_2, HbR, and HbT, seed-based FC maps were constructed in the conventional 0.009-0.08Hz frequency band using data acquired in the anesthetized state to compare to previously reported results [2]. These hemoglobin-based FC maps qualitatively recapitulated previously reported FC topography (Fig. 3.7).

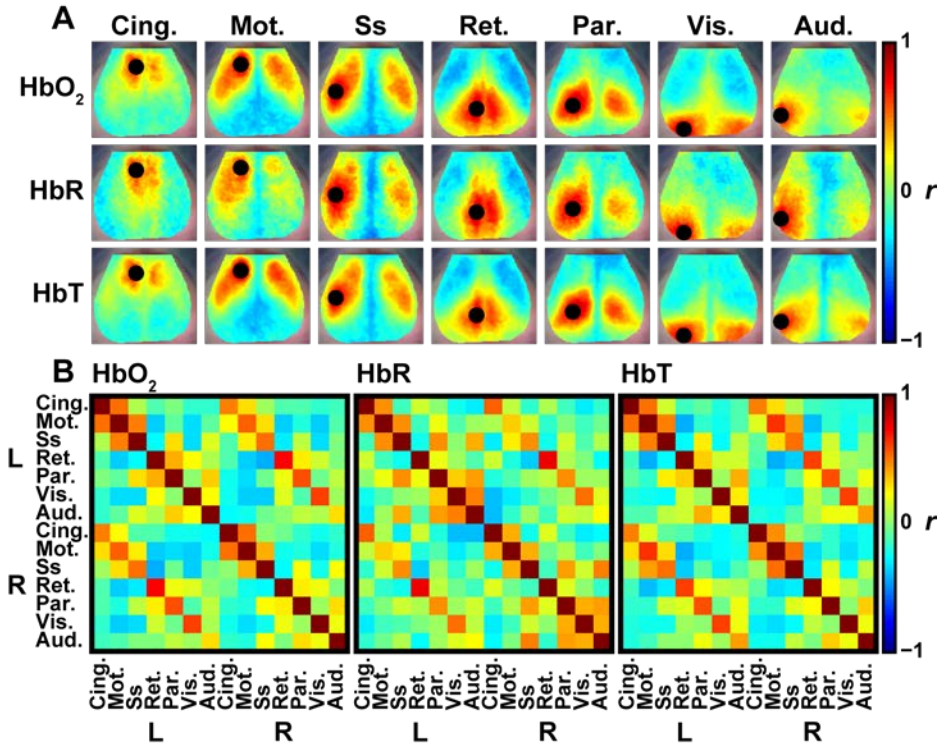

Figure 3.7. Seed-based functional connectivity maps and matrices constructed using spontaneous, infraslow hemodynamics. Group-level seed-based functional connectivity maps (A) and matrices (B) of infraslow (0.009-0.08Hz) spontaneous oxyhemoglobin (HbO_2), deoxyhemoglobin (HbR), and total hemoglobin (HbT) acquired in the ketamine/xylazine-anesthetized state.

Though the origins of the GCaMP6 and HbO_2 signals are distinct, they are associated via neurovascular coupling [70, 72]. Because of this, we wanted to examine the potential interaction between infraslow GCaMP6 and HbO_2 dynamics. By calculating the cross-correlation (with sliding delay) between the GCaMP6 and HbO_2 evoked responses to electrical hindpaw stimulation (Fig. 3.4), we measured the temporal delay of HbO_2 relative to GCaMP6 to be ~0.65s (Fig. 3.8A & B). For reference, we evaluated the same seed locations previously used for hemodynamic functional connectivity mapping [2] (Fig. 3.8C, top). Within the infraslow frequency band, GCaMP6 produced intact functional connectivity patterns (Fig. 3.8C, bottom) spatially qualitatively similar to concurrent HbO_2 maps (Fig. 3.8C, top), as well as to maps made using deoxyhemoglobin (HbR) and total hemoglobin (HbT) (Fig. 3.7). Next, to evaluate the potential relationship between spontaneous GCaMP6 activity and hemoglobin dynamics, we temporally shifted spontaneous GCaMP6 traces for the seven seeds by the 0.65s delay (from the hindpaw activation data) and then calculated correlation maps between the GCaMP6 seeds and the shifted HbO_2 data. The resulting maps (Fig. 3.8C, middle) have distinct patterns that look qualitatively similar to the within-contrast hemoglobin based functional connectivity maps (Fig. 3.8C, top). These results imply that both signals carry shared functional information, with GCaMP6 potentially containing predictive information of downstream hemodynamics.

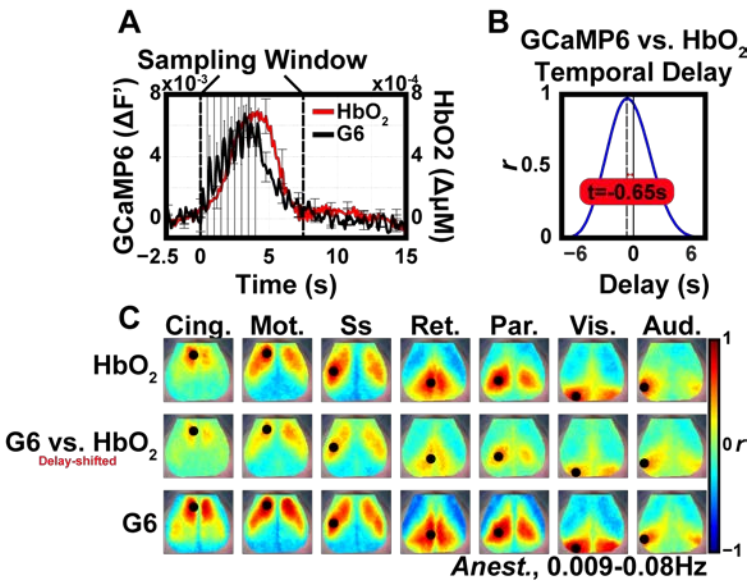

Figure 3.8. Intercontrast functional connectivity mapping using delay derived from somatosensory functional responses. Based on the temporal delay between evoked GCaMP6 and HbO_2 responses combined with similar observed infraslow FC structure, delay-shifted GCaMP6 likely shares functional network information with HbO_2. A) GCaMP6 (black) and HbO_2 (red) evoked responses to 2Hz 0.5mA electrical stimulation of left hind paw (see Fig. 3.4). Data from a sampling window spanning from approximately t=0s to t=7.5s were included in subsequent cross-correlational delay analysis. B) Cross correlation from the GCaMP6 and HbO_2 time courses in A) show a delay of 0.65s between responses. C) Top and Bottom: Seed-based group-averaged FC mapping in filtered (0.009-0.08Hz) anesthetized data using HbO_2 and GCaMP6. Spontaneous GCaMP6 and HbO_2 show similar functional network topography at low frequencies. Middle: Intercontrast FC maps using GCaMP6 seed traces against delay-shifted (0.65s) HbO_2 data. Infraslow correlation between spontaneous HbO_2 and GCaMP6 contrasts is optimized by removing the intersignal time shift between contrasts.

To establish the relationship between the magnitudes of the delay used to shift HbO_2 relative to GCaMP6, we calculated the similarities of the outputted intercontrast FC maps, parametric in delay magnitude, against the corresponding group-average infraslow HbO_2 FC map, which served as the ground truth for reference (Fig 3.9). For certain networks (e.g. visual, motor), spatial similarity between the intercontrast FC map and the HbO_2 reference image are maximized at a delay of approximately 1.5-2 seconds, whereas the similarity compared to the HbO_2 reference for other networks (e.g. auditory, retrosplenial) are monotonically decreasing and are thus maximally similar at a zero delay. It should be noted that more data are necessary to ensure that these networkwise differences are intact and not due exclusively to sampling variability.

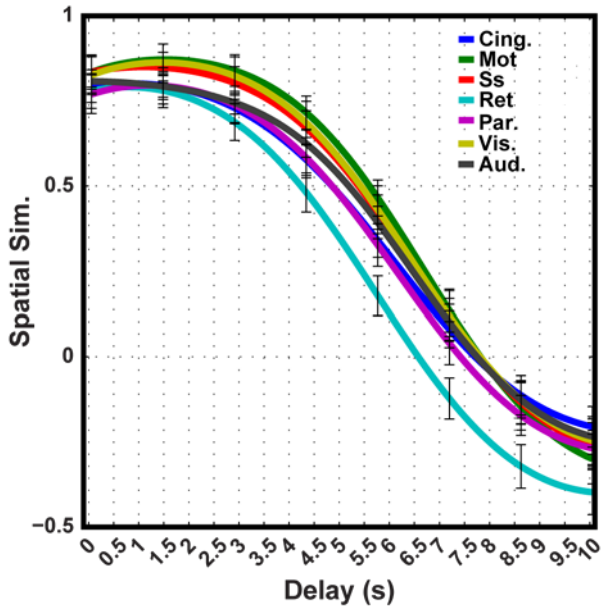

Figure 3.9. Spatial similarity of seed-based intercontrast functional connectivity maps parametric in delay. Spatial similarity between the constructed seed-based intercontrast FC maps and the corresponding HbO_2 maps, all constructed using anesthetized spontaneous data filtered from 0.008-0.09Hz. GCaMP6 seed traces were correlated with HbO_2 data shifted from 0 to 10 seconds in increments of approximately 0.12 seconds for all networks. By the 10 second delay, all

networks a highly reduced similarity. However, at shorter magnitude delays, some networks (e.g. motor) are more similar than the zero-shift images.

3.6 Propagating Waves in Spontaneous, Delta-Band GCaMP6 Activity in Anesthetized Mice

When examining pre-processed, delta-band spontaneous GCaMP6 image series acquired during the anesthetized state, a salient wave-like feature is prominent across all sessions (a representative 1.2s image series from one mouse can be seen in Fig. 3.10). Starting from the t=0 frame, there is an area of high activity (red) located in the anterior portion of the brain that travels backward through t=0.36s, before repeating from t=0.42s to t=1.2s. This phenomenon continues and is observable across all ketaminze/xylazine-anesthetized imaging sessions but is attenuated in wakefulness. Given this state-dependence and the occurrence in the delta frequency band (0.4-4.0Hz), it is likely that these waves are propagating delta-band waves associated with slow wave sleep and anesthesia.

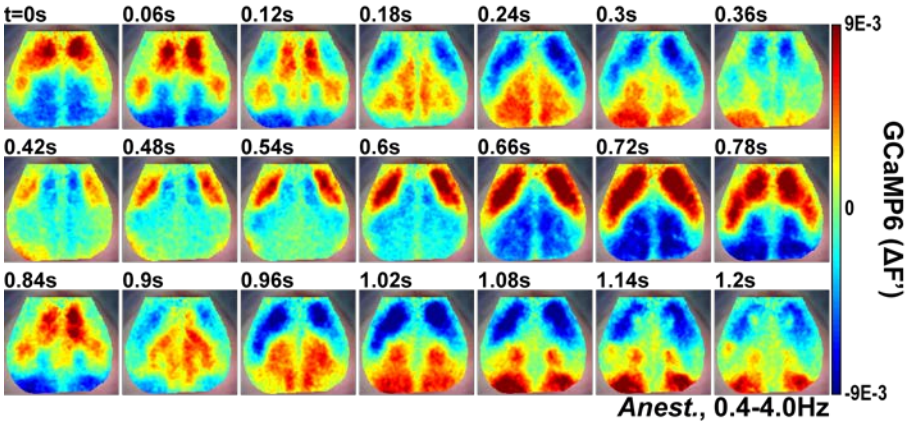

Figure 3.10. Image series of spontaneous, delta-band (0.4-4.0Hz) GCaMP6 activity from a representative anesthetized mouse. Consecutive frames from a 1.2 second duration image series of spontaneous GCaMP6 activity from one ketamine/xylazine-anesthetized mouse. Data are filtered from 0.4-4.0Hz. Note the anterior-posterior propagation areas of peak activity.

3.7 Delta-Band GCaMP6 Shows a Striking State-Dependence in FC Structure

To examine a potential dependence of GCaMP6 activity on state (anesthesia vs awake), we evaluated seed based functional connectivity maps of GCaMP6 in the higher 0.4-4.0Hz frequency band (Fig. 3.11). Under ketamine/xylazine anesthesia (Fig. 3.11, top row), GCaMP6 networks show an anterior-posterior network separation, with large regions of high magnitude correlations and anti-correlations arising across the cortex. In contrast, network correlation structure in the awake state (Fig. 3.11A, second row) exhibits higher spatial specificity for each network of interest. To quantify the degree of detail and localization, we thresholded using pixels with positive correlations >0.2 of the maximum correlation value in each image and then summed the remaining pixels to generate an score in units of estimate of area (here referred to as correlation area) and averaged these across all seven seeds. The mean correlation area in the awake state was 39.2% (std +/- 15.9%) smaller than that of the corresponding anesthesia maps. The difference images constructed between the group level anesthetized and awake functional connectivity maps (third row) show approximately the same overall topography in cingulate, motor, somatosensory, retrosplenial, and visual networks, pointing to a loss of specificity in seed-based functional connectivity maps in the anesthetized state. This is further supported by the many common structures across the pixelwise T-statistic maps (Welch's t-test). Finally, horizontal line profiles through the center of each seed for both the awake (red) and anesthetized (blue) functional connectivity maps show higher spatial focality (measured using reductions in ipsilateral and contralateral full width at half maximum, Table 3.1) in cingulate, motor, somatosensory, retrosplenial, and visual networks in the awake state.

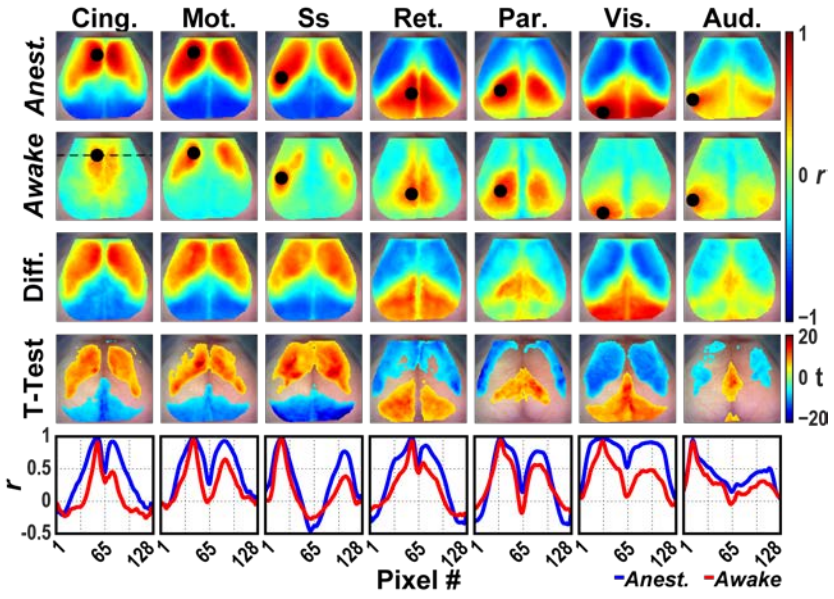

Figure 3.11. Group-level seed-based GCaMP6 functional connectivity maps constructed from delta-band spontaneous activity acquired in the anesthetized and awake states. A) Seed-based FC maps for seven canonical functional networks in anesthetized and awake GCaMP6 mice (n=7) at delta-band frequencies. Under anesthesia (top), delta activity (0.4-4.0Hz) drives a strongly correlated/anticorrelated network structure between anterior and posterior brain regions that is not observed in awake animals (second row). This high magnitude correlation feature is preserved in the difference images (third row) and after performing pixelwise t-tests and thresholding the T-statistic maps at a Bonferroni adjusted α=3.1e-6 (fourth row). Together, these show that the topography of FC maps in the anesthetized state is largely independent of seed-based network structure. Finally, horizontal line profiles through the center of each seed show higher ipsilateral and contralateral focality in the awake (red) FC maps compared to anesthetized (blue) maps (fifth row and table in Table 3.1).

Table 3.1. Ipsilateral and contralateral full width at half maximum values of horizontal line profiles sampled from group-level seed-based, delta-band GCaMP6 functional connectivity maps in the anesthetized and awake states.

	Ipsilateral FWHM			Contralateral FWHM		
Network	Anest.	Awake	P-value[a]	Anest.	Awake	P-value[a]
Cing.	975 (155)	643 (78)	5.7e-12*	1362 (185)	1009 (252)	2.3e-09*
Mot.	1005 (157)	726 (88)	4.4e-10*	1872 (258)	1595 (328)	0.00010*
Ss	1116 (166)	792 (64)	8.5e-11*	1743 (341)	1518 (500)	0.014
Ret.	966 (273)	751 (180)	0.00046*	1860 (451)	1421 (546)	0.00028*
Par.	1269 (425)	1050 (334)	0.015	2157 (432)	2217 (601)	0.314
Vis.	2727 (712)	1572 (687)	9.1e-09*	3561 (509)	3096 (410)	0.00013*
Aud.	900 (429)	801 (141)	0.131	2712 (1007)	2356 (748)	0.062

FWHM, full width at half maximum. Mean (SD) in μm are shown. [a]p-values determined using Welch's t-test. *Significant difference using a Bonferonni-corrected α=0.007 threshold.

Visualized in matrix form (Fig. 3.12), the pairwise functional network connections under anesthesia (Fig. 3.12, left) show clustering of positive correlations in anterior networks (cingulate, motor, and somatosensory) and negative correlations in posterior networks (retrosplenial, parietal, visual, and auditory), whereas awake animals (Fig. 3.12, right) exhibit stereotypical high correlation strength only in the off-diagonals. Note the FC structure over the delta band during wakefulness is consistent across all mice (Supplementary Fig. 3.1).

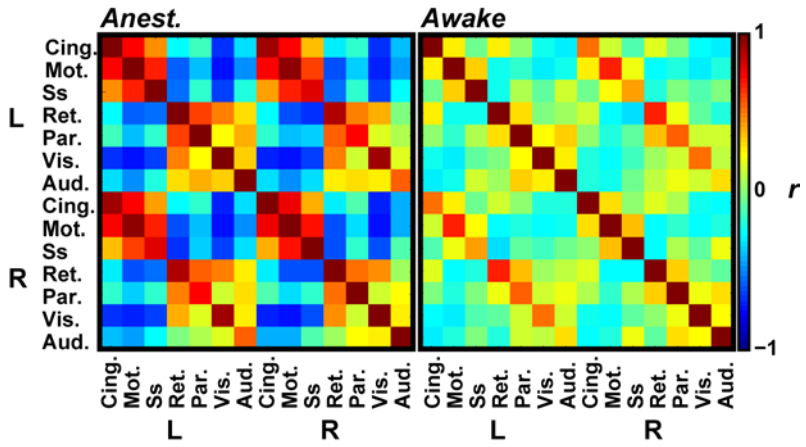

Figure 3.12. Group-level seed-based GCaMP6 functional connectivity matrices constructed from delta-band spontaneous activity acquired in the anesthetized and awake states. Regional correlation coefficients between each seed reveal heterogeneous connectivity structure within each contrast across different states. Clusters of networks are present in the anesthetized matrix (left), including between cingulate, motor, and somatosensory networks that are diminished in the awake mouse (right).

Next, seed-based coherence and imaginary coherence maps were made for both the awake and anesthetized states in delta-band GCaMP6 data. Coherence can be intuitively understood as correlation of spectral content. The high global coherence values in the anesthetized maps describe a common shared spectral content across both anterior and posterior cortical regions. This feature is largely absent in the awake coherence maps (Fig. 3.13A, bottom row), wherein the seed-based maps are highly spatially-specific. The imaginary coherence images (Fig. 3.13B) show similar behavior, with regions of high imaginary coherence implying shared spectral content at non-zero time delays (relative to each respective seed). Collectively, these results point to a widespread

phenomenon with spatially-independent, stable spectral content that exists across non-zero time delays compared to each seed, likely propagating delta-band waves.

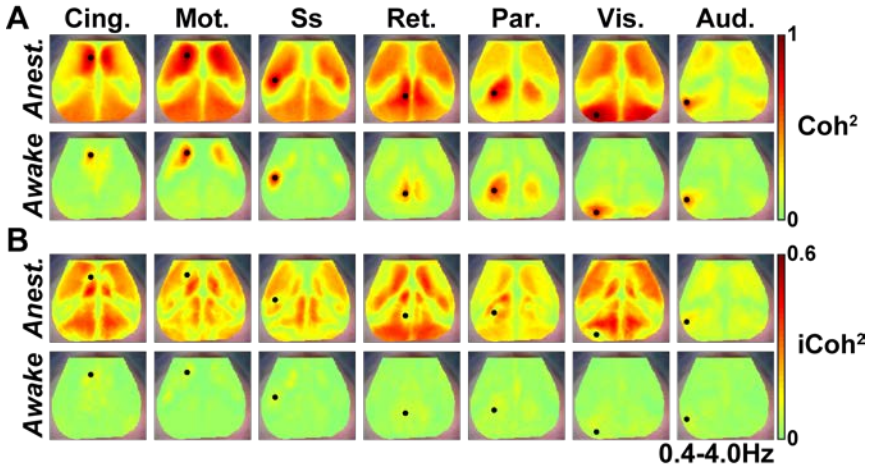

Figure 3.13. Group-level seed-based coherence and imaginary coherence maps constructed using spontaneous, delta-band GCaMP6 activity in the anesthetized and awake states. Seed-based coherence (A) and imaginary coherence (B) maps for the group-level ketamine/xylazine-anesthetized (top row) and awake (bottom row) spontaneous GCaMP6 data. There is a high global coherence and imaginary coherence across seeds that is absent upon wakefulness.

3.8 Strong Cortical Delta-Band Activity is Associated with Anterior-Posterior GCaMP6 Dynamics and FC Structure

Compared to the FC structure of GCaMP6 during wakefulness, FC maps under anesthesia largely contain strong anti-correlations between anterior and posterior brain structures (Fig. 3.11). These anti-correlations might be indicative of coherent propagating waves of spontaneous GCaMP6 activity over the anterior-posterior axis. To determine if our model and system are sensitive to these dynamics, we examined the frequency content of global spontaneous GCaMP6 activity in a

representative mouse under ketamine/xylazine anesthesia and while awake (Fig. 3.14). A phenomena commonly reported in the sleeping and anesthetized brain is the presence of prominent propagating slow-wave delta activity [67]. The GCaMP6 spectra of mice under anesthesia (Fig. 3.14, black trace) reveal a peak centered at ~1.5Hz that is absent upon wakefulness (Fig. 3.14, gray trace), which is consistent with previous electrophysiological studies reporting delta-band activity over this frequency range [61]. Further, the state-dependence of delta activity exhibited in GCaMP6 dynamics is recapitulated in the simultaneously-acquired global field potential EEG data (anesthetized: dark green, awake: light green).

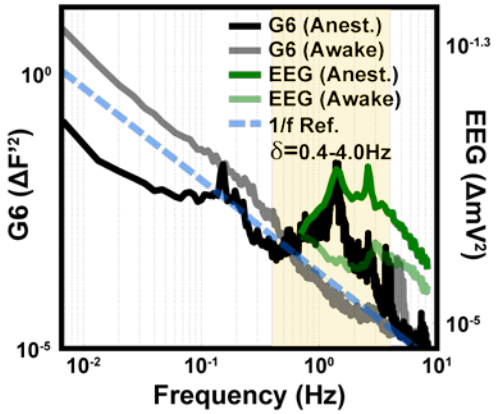

Figure 3.14. Frequency spectra of spontaneous GCaMP6 activity and concurrently acquired EEG sampled from a representative mouse in the anesthetized and awake states. Frequency spectra from the whole brain from a representative mouse. The presence of a peak at ~1.5Hz in both the anesthetized GCaMP6 (dark black) and EEG (dark green) corresponds increased delta band (0.4-4.0Hz) activity in the brain under deep, slow-wave sleep. Note that this peak is absent when the mouse is awake (GCaMP6, transparent black, EEG, transparent green).

In order to better understand the observed state-dependent GCaMP6 FC structure, we examined the delay topography of the GCaMP6 signal by calculating the pixelwise lag relative to the whole-

brain signal (Fig. 3.15 & Fig. 3.16). The time shift that maximizes the cross-correlation between each pixel's time series and the whole brain signal is plotted at every pixel to construct a time delay map. At the group level (Fig. 3.15), the statewise contrast observed in Fig. 3.11 is prominent, with somatomotor regions tending to lead the brain by up to 0.08s and visuoparietal areas lagging by a comparable magnitude. This temporal separation across the cortex could underlie the observed anterior/posterior structure found in the functional connectivity maps of GCaMP6 activity in anesthetized animals (Fig. 3.11).

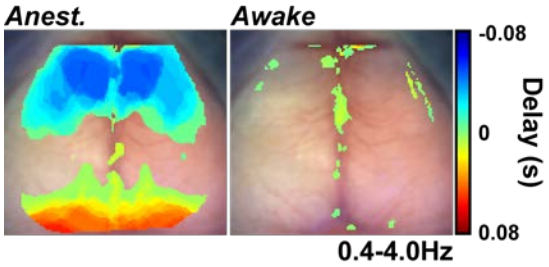

Figure 3.15. Group-level pixelwise delay maps in the anesthetized and awake states constructed using spontaneous, delta-band GCaMP6 activity. Group-wise delay maps in anesthetized (left) and awake (right) mice (n=7). Spontaneous activity in anesthetized and awake mice reveals regional temporal delay structure with respect to the whole brain signal. Maximum cross-correlation between the whole brain signal and each pixel's timeseries were calculated across the FOV. The map from anesthetized mice (left) show a temporal separation along the anterior-posterior axis of the brain, with anterior somatomotor regions leading the whole brain signal by <=0.06s and posterior visuoparietal areas lagging the whole brain signal by <=0.06s. This time shift is in agreement with the striking correlated/anti-correlated structure in the delta band FC maps. This structure is no longer intact in awake mice.

Finally, to illustrate the changes in delay and functional connectivity structure that depend on state, we examined spontaneous GCaMP6 activity in a mouse transitioning from anesthesia to wakefulness across six consecutive five-minute epochs (Fig. 3.16). In the first epoch (E1), the mouse shows an anterior-posterior delay structure (Fig 3.16, top), with cingulate regions leading the whole brain signal by ~0.08s and visual/parietal regions lagging by ~0.08s. As the mouse wakens (determined by the attenuation of delta-band power, peak at ~1.7Hz, Fig. 7C spectrogram), this topography deteriorates (Fig. 3.16, top, transition from E2 to E3). The corresponding functional connectivity map constructed using a left visual seed is shown for each epoch (Fig. 3.16, middle section, top row). To improve SNR when creating average functional connectivity maps (Fig. 3.16, middle section: top row) and enable statistical testing using paired t-tests (Fig. 3.16, middle section: bottom row), each five-minute epoch was divided into ten 30s windows. This window length was selected based on the observed convergence in spatial similarity of functional connectivity maps constructed using at least 30s of spontaneous data compared to the group average reference (Fig. 3.6). During wakefulness, the correlation maps show smaller, more detailed regions of reduced correlation magnitude, both ipsilateral and contralateral to the seed, as compared to the maps during anesthesia. Successive difference maps calculated for each epoch compared to E1 show parietal cortex differ the most between across this transition from anesthesia to wakefulness. There is also a subtle but visible difference in cingulate cortex between E1 and the later epochs. It should be noted that when implementing a seed-based iterative parcellation strategy across this state transition, there is a subtle restructuring of functional parcels, especially in posterior regions, in E6 compared to E1 (Supplementary Fig 3.2A). It is possible that in the absence of delta-band wave propagation, the brain will tend to parcellate into truer functional parcels. At the group level, parcellation maps during wakefulness of much more prominent medial regions

(e.g. retrosplenial cortex) that were “masked” under anesthesia (Supplementary Fig. 3.2B). We plotted T-statistic maps (thresholded at q<0.001 after false discovery rate adjustment) constructed from pixelwise paired t-tests between E1 and all subsequent epochs recapitulate these findings (Fig. 3.16, middle portion: bottom). The anterior, cingulate region leads the brain during anesthesia (E1, Fig. 3.16, top), which is consistent within the difference T-statistic maps of functional connectivity during the awake epochs (E5 and E6). The boundary of maximum delay value from this cingulate network (E1, Fig. 3.16, top) is overlaid on the T-statistic map in E6, showing the agreement across both analysis strategies.

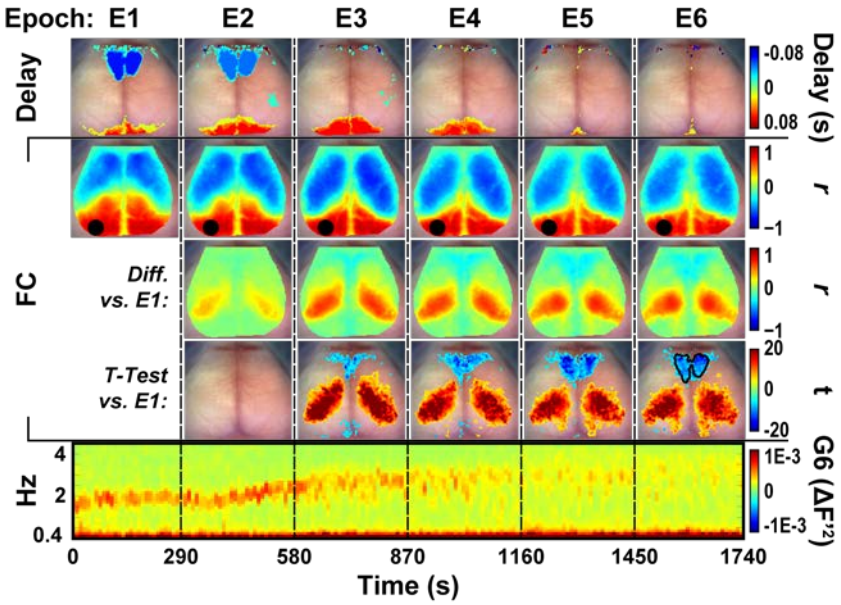

Figure 3.16. Pixelwise delay and functional connectivity analyses using spontaneous GCaMP6 activity during a state transition (anesthetized to wakefulness) from a representative mouse. Top: Delay maps from consecutive 300s epochs from one mouse as it transitions out of anesthesia to awake reveals a loss of anterior-posterior delay structure across time. Middle section: FC maps for a left visual seed from each epoch (top row), difference images between each successive epoch and E1 (middle row), and pixelwise T-statistic maps after performing paired t-tests between E1 and each other epoch (bottom row). The boundary of the area

of maximum delay in the anterior, cingulate network in the delay map in E1 (top row) is overlaid on the E6 T-statistic map for reference. These data show that the correlation magnitude of the parietal region differs across state and that there is agreement across delay and FC analyses in the implicated cingulate network. All analysis was performed after dividing each 300s epoch into ten 30s windows. Bottom: Spectrogram over the delta frequency band (0.4-4.0Hz) from each epoch showing the loss of delta-band activity (peak at ~1.7Hz) with time across epochs.

3.9 Supplemental Figures for Chapter 3

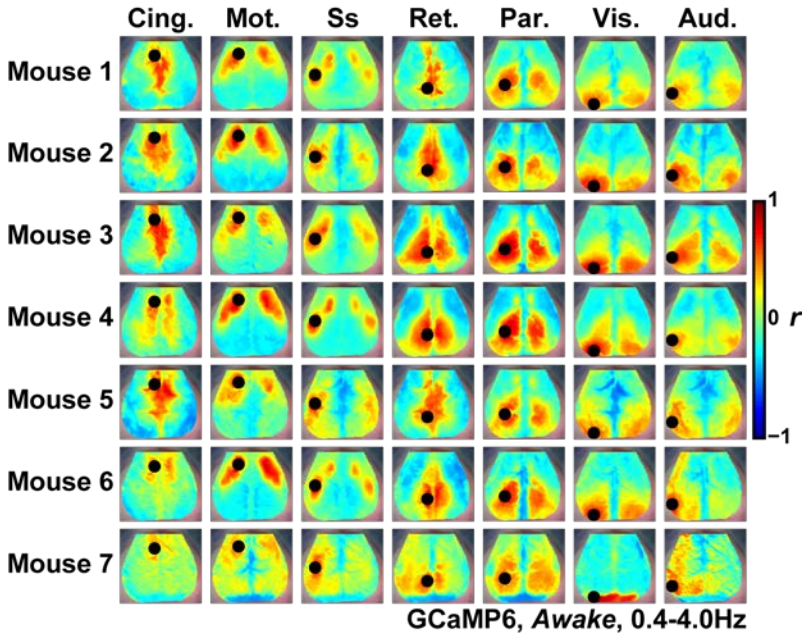

Supplementary Figure 3.1. Seed-based, delta-band GCaMP6 functional connectivity maps from seven individual awake mice. GCaMP6 functional connectivity maps of all 7 individual mice in the imaging cohort, filtered over the delta (0.4-4.0Hz) frequency band. The same canonical network seeds used in Figures 4 & 5 were applied here. Data shown are acquired in the awake state.

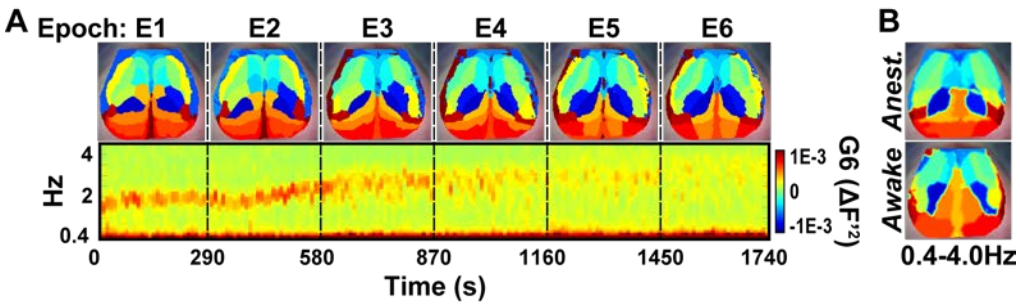

Supplementary Figure 3.2. Parcellation maps constructed using spontaneous, delta-band GCaMP6 data during a state transition and during both the anesthetized and awake states (at the group-level). A) Top: Parcellation maps from consecutive 300s epochs from one mouse as it transitions out of anesthesia to awake. Bottom: Spectrogram over the delta frequency band (0.4-4.0Hz) from each epoch showing the loss of delta-band activity (peak at ~1.7Hz) with time across epochs. B) Spatially-smoothed group-wise parcellation maps in anesthetized (top) and awake (bottom) mice (N=7). Parcellation maps were calculated for each 5 minute imaging session (within state) and the mode for each pixel was determined across sessions. The mode, corresponding to the most frequently assigned parcel selected for each pixel, was plotted for all pixels to construct the final group-level images

Chapter 4: DISCUSSION

4.1 Overview of Findings

The goal of this thesis was to establish the existence of FC patterns in spontaneous calcium activity and determine whether they are modulated by state. For functional mapping, calcium dynamics have the appeal of being faster and more directly related to neuronal activity than hemoglobin dynamics. Specifically, we imaged spontaneous calcium activity in mice expressing GCaMP6 driven by the Thy-1 promoter. The neural origins of the fluorescence signal were established first through electrical stimulation of the hindpaw, in which the fast positive response of the corrected GCaMP6 signal to each pulse presentation indicated both the neuronal origin and also the utility of the correction for absorption transients (Fig. 3.4). Resting GCaMP6 activity also exhibited spatio-temporal correlative structure reflecting functional network connectivity within an infraslow frequency band (0.009-0.08Hz) and also at a higher frequency band (0.4-4.0Hz) that captures delta activity (Fig. 3.11). Spontaneous GCaMP6 data at this higher frequency band can provide stable, consist FC maps with as little as 30s of imaging (Fig. 3.6). Additionally, under resting state conditions in anesthetized mice, simultaneously-acquired EEG independently confirmed that the GCaMP6 signal contained a high-amplitude peak in delta-band that was absent in awake mice (Fig. 3.14). Moreover, state-dependent differences in apparent FC structure in delta-band GCaMP6 activity appeared to be driven by the underlying temporal delay topography of the brain (Fig. 3.15 and Fig. 3.16).

4.2 Functional Connectivity Stationarity and Sampling Variability

In attempting to establish a floor for the amount of spontaneous delta-band GCaMP6 data necessary to construct typical FC maps, we observed that seed-based functional connectivity maps

converge on a spatially similar structure to that of group-averaged data (made using 300 second sessions) with as little as 30 seconds of data. We also observed, while these 30 second windows were relatively stationary (Fig. 3.6), there was a slight drift in spatial similarity. This could be due to neurophysiological changes arising across the duration of the run. However, it should be noted that this analysis does not account for or examine the effects of sampling variability and physiological stability separately in isolation. Laumann et al. have reported that for short time windows (e.g. <300 seconds), the variance in functional connectivity Pearson correlation measurements is attributable to sampling error and is inversely proportional to time window length [73]. More recently, it has been reported that fluctuating arousal state and sleep can drive non-stationarity in functional connectivity structure, even after accounting for the variance in FC maps contributed to by motion and sampling variability [74]. The variability in the similarity of the sliding 30 second window of spontaneous GCaMP6 data (sampled from left motor cortex; Fig. 3.6) compared to the group average image could be driven by these artifacts. Future studies are needed to thoroughly examine the stability and stationarity of the GCaMP6 and the confounding effects of motion.

4.3 Inherent Functional Connectivity across Contrast, Frequency, and State

The correspondence between functional connectivity maps of HbO_2 and GCaMP6 over the infraslow frequency band (Fig. 3.8C, top and bottom) is in agreement with previously reported observations that measures of spontaneous calcium, local field potentials, and HbO_2 low frequency oscillations (<0.1Hz) are correlated across the rat cortical vascular tree [8]. Collectively, these findings further reinforce the utility of functional hemodynamic measures as surrogates for neuronal activity at frequencies <0.5Hz. Interestingly, the similar functional connectivity features

in the infraslow FC maps and the ability to recover functional connectivity structure in delay-shifted spontaneous HbO_2 data using inter-contrast functional connectivity analysis (Fig. 3.8C, middle) point to an inherent shared network topography across both calcium and hemoglobin dynamics. This is further supported by the high spatial similarity observed across network in all constructed intercontrast FC maps compared to the corresponding HBO_2 images, even at zero delay shift (Fig 3.9). The inter-contrast results also strongly suggest that the spontaneous calcium and hemoglobin are synchronized. Furthermore, the general superficial similarity in GCaMP6 FC structure over both frequency bands and across states-of-consciousness (Fig. 3.11) implies a base FC structure, in that at least some components of the underlying functional network architecture exist independent of state and across a wide band of frequencies. These reports add to a growing literature on stable, stereotypical FC network structure, observed using a fluorescent glutamate sensor in both isoflurane-anesthetized and awake mice at frequencies up to 12Hz [26] and using 128-channel electrocorticography in ketamine/medetomidine-anesthetized and awake macaques [75]. However, upon calculating difference images and using pixelwise statistical tests, the state-dependent changes in functional connectivity structure become much more apparent. At the group level, seed-based functional connectivity maps created using anesthetized spontaneous data show a topography that is relatively independent of network seed (Fig. 3.11, third and fourth row) other than a sign change as the seeds move along the anterior to- posterior axis. Across the anesthetized data, there exists a highly clustered binary structure with high magnitude correlations and anticorrelations that persists even after subtraction of the more focal and spatially specific awake maps. Similar topography exists in the corresponding seed-based coherence maps. The anterior and posterior correlative structure combined with the high coherence in both clusters points to equivalent neural activity that is out of phase along the anterior-posterior axis. When examining

an individual mouse transitioning from anesthesia to wakefulness, cingulate and parietal areas are most different with maximally attenuated delta-band power (Fig. 3.16). This parietal region, located in the transition zone between the anterior and posterior network clusters, has been shown to act a sink for activity induced multi-modal sensory stimulation, imaged *in vivo* in mice using a voltage-sensitive dye [24]. It is possible that as a sensory integration center, it is highly synchronized with the activity of the visual cortex during anesthesia.

4.4 Delay Topography and Functional Connectivity

In addition to patterns of functional connectivity, the temporal delay topography of the cortex (Fig. 3.15 and Fig. 3.16) was also dependent on state. Under anesthesia, the GCaMP6 activity over the delta frequency band propagated from anterior regions (e.g. motor) to posterior regions (e.g. visual), and is consistent with previous observations in sleeping humans and anesthetized mice [67, 76]. These travelling oscillatory waves have been suggested to facilitate memory consolidation during natural sleep [77]. Importantly, ketamine and xylazine (used here), compared to other common anesthetics, has been shown to best mimic natural sleep, especially in the context of the sleep slow oscillation [60]. The strength of the oscillations likely underlies the strong correlations and anti-correlations seen in the functional connectivity maps of the delta frequency band (Fig. 3.11). The temporal separation observed across the cortex drives activity in anterior somatomotor networks to be more out of phase with posterior visual/parietal regions (Fig. 3.15), increasing the apparent strength in contralateral homotopic connections while also increasing the anti-correlation magnitudes between somatosensory and parietal regions. Human fcMRI studies have shown that FC structure can be a consequence of the delay topography while the reverse might not necessarily hold true [78]. It is therefore possible that this prominent propagating wave

of delta-band oscillations is superimposed with spontaneous activity associated with functional network connectivity structure (e.g. that seen in wakefulness), and provides the increased correlation magnitudes and anterior-posterior clustering unobserved in awake animals. This concept is supported by recent work in isoflurane-anesthetized transgenic Emx1/GCaMP3 mice in which traveling transient neuronal coactivations occurred in areas exhibiting high functional connectivity [79]. In this thesis, we observed that the same anterior, cingulate regions that lead the brain in the delay maps (Fig. 3.16, top, E1 & E2) are also the regions of maximal difference in the functional connectivity structure across a transition from anesthesia to wakefulness (Fig 3.16, middle section: bottom, E5 & E6). Interestingly, the delay structure present over the delta band under anesthesia was not observed in awake animals (Fig. 3.15). However the current analysis was limited by the sampling rate (16.8 Hz) and would not be sensitive to delays shorter than approximately 0.06 seconds.

4. 5 Related Studies in the Field

While there are studies of evoked responses with macroscopic imaging of GECIs, there are relatively few with GECI's that explore either functional connectivity [7, 50, 51, 79] or other analysis of calcium dynamics (e.g. functional hyperemia) [80] Of the studies reporting correlative functional structure in spontaneous calcium dynamics, they are either limited to one state of consciousness and/or to poorer performing GECIs [7, 50, 79]. Collectively, though, these previous reports largely support the results of the present thesis. For example, while Vanni et al. demonstrated mesoscale somatomotor functional connections in spontaneous calcium activity, using an isoflurane-anesthetized Emx1/GCaMP3 mouse model, which resemble the somatosensory and motor seed-based functional connectivity maps of the present thesis [50].

Recently, Silasi and colleagues reported similar homotopic functional connectivity structure in seed-based maps in awake and isoflurane-anesthetized mice. They observed an increase in network focality and reduction in correlation magnitude upon wakefulness, analogous to the results reported here, despite the difference in selected anesthesia (isoflurane vs. ketamine/xylazine), frequency content of spontaneous data (1-10Hz vs. 0.4-4.0Hz), and amount of data included in analysis (approximately 35 minutes of awake imaging data from 7 mice and approximately 10 minutes of anesthetized data from 2 mice compared to the 130 minutes of anesthetized data and 225 minutes of awake data across 7 mice, acquired within the same imaging session, in the present thesis) [51].

4.6 Limitations

There are several limitations to the current thesis that support the need for further work. The ratiometric method implemented here for removing confounding absorption of GCaMP6 fluorescence emission by hemoglobin could be additionally optimized. For example, to remove confounding absorption of in situ fluorescence by glycation end-products in porcine skin models of diabetes, Hull and colleagues estimated two scaling parameters used in their ratiometric correction that minimized intra-subject fluorescence variability across sessions and maximized the expected correlation between age and fluorescence intensity [81]. While the correction method implemented here is effective at removing artifactual absorption dynamics (e.g. the negative uncorrected raw GCaMP6 response to left hindpaw stimulation, Fig. 3.4B), further optimization could focus on using a physiologic marker (e.g. pulse) that would provide independent validation of the correction. Additionally, flavoproteins are autofluorescing metabolites that display elevated fluorescence emission with increasing oxidative metabolism [35]. Problematically, their

fluorescence spectra overlap with that of GCaMP6 (excitation at λ=460 and emission at λ=520). However, their temporal dynamics are distinctly slower than those of calcium. In particular, it has been shown that compared to flavoprotein autofluorescence, GCaMP3 has a significantly faster onset (GCaMP3: 0.28s vs. flavoproteins: 0.62s; p=0.002) and time to peak (GCaMP3: 0.65s vs flavoprotein: 1.11s; p<0.001) in response to a 1s hindlimb stimulation at 100Hz [50]. Similarly, in vitro studies in rat cortical slices showed an evoked calcium response (measured using the rhod-2 calcium indicator) to 1s 20Hz electrical stimulation peaking ~1.5s before the measured flavoprotein autofluorescent response [34]. Thus, the slower temporal characteristics of flavoprotein dynamics compared to calcium transients, at least over higher frequencies (e.g. delta-band analyses in this thesis), will likely result in little contamination of the GCaMP6 signal. Finally, Thy1 expression patterns determine the effective field-of-view of our imaging system and can vary with age, sex, filial generation, and genetic background [82]. The cohort of mice in the present thesis share the same background and are matched for age and sex. However, mice were either F1 (n=3) or F2 (n=4) relative to their F0 breeding pair from The Jackson Laboratory (https://www.jax.org/). Despite this difference, results were assessed at the individual mouse level and were qualitatively recapitulated across the group.

4.7 Future Studies

Future studies could take advantage of concurrent GCaMP6 and hemodynamic imaging to study diseases that impact neurovascular coupling by providing evidence on the sequence of neurodegeneration and vasculopathy underlying these conditions. In this thesis, we found a high concordance between calcium and HbO_2 at infraslow frequencies. These were in healthy adult mice in which neurovascular coupling is relatively intact and spatially homogenous across the

cortex. However, in a wide variety of diseases such as stroke [3, 44] and Alzheimer's disease (AD) [4, 83, 84], neurovascular coupling and hemodynamic functional connectivity can be compromised or modulated. For example, in a mouse model of AD, a decline in hemodynamic functional connectivity was found to be driven, in part, by deposition of amyloid-β (Aβ) plaques [4]. This AD-associated functional disruption was restored upon immunotherapy with HJ6.3 antibody that limits formation and growth of new Aβ plaques [5], with treated mice showing mildly improved performance in a spatial learning task. A concurrently-acquired imaging probe of neuronal activity (e.g. GCaMP6) could provide mechanistic information underlying these observed cognitive changes. Furthermore, AD-related Aβ accumulation and deposition has been recently shown to disrupt delta-band slow wave coherence and propagation [85], providing a fitting target of study for the multi-modal imaging system described here.

4.8 Summary

In summary, GCAMP6 activity reveals functional connectivity structure over a frequency range (from 0.009 Hz to >4Hz) higher than the canonical functional connectivity band (0.009 to 0.08 Hz) that is state-dependent. Calcium-based spontaneous mapping of functional connectivity is faster and more directly coupled to neural activity than hemoglobin-based mapping of functional connectivity. Further, the calcium signal can be targeted and localized to specific types of cells providing an exquisitely specific method for detailed mapping of mesocopic connectivity patterns. Finally, combined GCaMP6 and hemodynamic imaging will enable the dissociation of changes in ionic- and hemodynamic-based networks and neurovascular coupling and provide a framework for subsequent studies of neurological disease such as stroke.

Chapter 5: CONCLUSIONS

5.1 Going Forward

Building off the methods and results described in this dissertation, there are a number of different avenues to pursue next, spanning topics that attempt to address disease pathology (e.g. narcolepsy) or fundamental architectural questions of the brain (e.g. delay topography).

5.1.1 Sleep and Narcolepsy

Given the ability of the described imaging session to visualize phenomena directly associated with sleep state, there is promising potential in extending this technique to the study of alternative sleep and anesthetic states as well as to sleep disorders. Steriade and colleagues have reported a delta-band frequency content dependence on anesthesia. Specifically, common anesthetics impact the "up" state depolarization envelope to varying degrees, subsequently impacting the frequency at which delta-band oscillations occur. Functionally, this becomes especially important given the different mechanisms of action of these anesthetics. For example, ketamine is a glutamate receptor (NMDA) antagonist, whereas dexmedetomidine is an α2-adrenergic receptor agonist, and isoflurane's anesthetic effect is thought to be mediated by antagonizing NMDA receptors or activating $GABA_A$ receptors [86]. Not only would this *in vivo* GCaMP imaging system allow for characterization of the potential influence of each of these anesthetics on the behavior of delta wave propagation, but it would also allow study of the effects of these anesthetics given their mechanistic and neuropharmacological differences. For example, a fluorophore expressed at glutamatergic synapses would be selectively impacted by ketamine compared to the potentially more indirect effect of the adrenergic agonist dexmedetomidine. Moreover, these anesthetics can strongly influence the cardiorespiratory system of mice (e.g. ketamine/xylazine causes significant

bradycardia, isoflurane decreases respiratory rate) [87]. The potential effects of these anesthetics on reported functional neuroimaging results must be established, especially given their commonality in rodent imaging studies. Broadly, the extent that anesthesia is pharmacologically modulating functional connectivity network topography and delay structure should be characterized.

Because of the aforementioned potential confounding effects of anesthesia, the mouse brain in natural sleep is likely the ideal model to study the state-dependence of functional connectivity structure. Though anesthetics, especially ketamine, are considered good models of slow wave sleep, conclusions from sleep studies that implement anesthesia are limited in the extent that they can be translated to sleep phenomenology. We have recently begun designing and carrying out a preliminary study to address these questions. The proposed study includes imaging GCaMP6 in wakefulness, natural, sleep, and a set of common anesthetics (ketamine/xylazine, isoflurane, and dexmetadomodine). Furthermore, the study includes both concurrently acquired EEG as well as EMG to confirm state of arousal. The next steps would be to use this approach to study sleep disorders, specifically narcolepsy. Narcolepsy is a disorder characterized by excessive daytime sleepiness, cataplexy, and fragmentation of sleep/wakefulness driven by a loss of orexin/hypocretin-expressing neurons of the hypothalamus. A double null mutant mouse model lacking both the orexin 1 receptor (OX1R) and orexin 2 receptor (OX2R) provides a reasonable model of narcolepsy-like symptomatology. A recently described doxycycline (DOX)-inducible model of narcolepsy, in which the presence of DOX reduces the number of orexin neurons, allows for nuanced control of orexin neuron population as well as age of onset (narcolepsy has a postpubertal onset in humans) [88]. This is especially powerful given that it allows for pre-onset imaging data to be acquired as a control timepoint. Because the extent of cortical network

involvement in the orexin system that underlie the narcolepsy phenotype is unknown, a bigenic mouse model that is OX1R/OX2R null and expresses GCaMP6 would provide pertinent information as to the pathology of narcolepsy, potentially driving a route to effective therapeutic interventions.

5.1.2 Projection-based Delay Analysis

The delay topography results observed in the resting-state GCaMP6 data over the delta frequency band across states and during a state transition points to the potential sensitivity of this approach to network reorganization. Mitra et al., have shown that “lag threads”, sequences of propogated activity, reflect neuronal processes rather than hemodynamic delay and potentially underlie spontaneous BOLD oscillations and subsequently-created resting-state functional connectivity networks [78, 89]. They have recently shown that the delay structure is sensitive to changes associated with Autism Spectrum Disorder (ASD) when compared to that of healthy controls [90]. Not only where these changes, observed in frontopolar cortex, occipital cortex, and putamen, associated with behavioral measures relevant to ASD diagnosis, but resting-state functional connectivity showed no groupwise differences. Similarly, this propagation analysis method has been shown to be sensitive to state of consciousness (wakefulness and slow-wave natural sleep) in humans, results that are recapitulated by those in this dissertation [68]. The combined GCaMP6 and hemodynamic imaging system described here permits the pursuit of more extensive propagation and delay analysis to examine the state- and frequency-dependence of delay topography and constituent lag threads. Components of the approach implemented by Mitra and colleagues (e.g. parabolic interpolation to improve effective sampling rate, lag projection map

construction on global-signal regressed resting-state data versus the non-regressed approach used here, etc.) will likely provide more striking statewise delay differences than reported here.

5.1.3 Neurovascular Coupling and Hemodynamic Response Functions

The fluorescent optical probes detailed in Chapter 1 provide an exciting opportunity to track synaptic activity throughout the cortex, with each probe providing complementary neurophysiological information. In order to truly begin to map the interplay across all stages believed to be part of neurovascular coupling (Fig 1.1), a number of methodological issues must be addressed. For example, the GCaMP fluorescence spectra overlap with that of FAD autofluorescence (~470nm excitation, ~530nm emission). If they can be concurrently imaged, one would be able to relate spontaneous metabolic fluctuations coupled to aerobic respiration to ionic transients. A possible solution is the use of recently developed CaM-calcium indicators that have different excitation wavelengths (e.g. >560nm). RCaMP1 (excitation at λ=575nm and emission at λ=610) has been recently engineering and provided SNR and kinetics on par with GCaMP6 [91]. These can be accommodated in the imaging system by use of multi-pass band filters or by using a high-speed filter wheel that is synced to switch to adjacent filter positions in the presence of respective excitation LED. Alternatively, a multi-camera array could also be implemented, similar to the system described by Vazquez et al. [7], but with required filers in different optical paths of the separate cameras. In this manner, it would be possible to gather information from hemodynamics (OIS), ionic transients (CaM), metabolism (FAD/NADH), and electrophysiology (VSDs). This also enables the acquisition parameters of each camera to be tuned for the specific contrast it is acquiring. For example, higher on-chip spatial binning in a CCD would increase SNR and potential frame-rate, parameters that may be useful for endogenous fluorophores with fast

kinetics. With this data, one would have biomarkers of a number of processes involved in NVC and would be able to use them to not only track disease mechanisms, but also use these contrasts in functional mapping approaches.

This becomes especially important if attempting to establish a response function between each pair of these contrasts. Logothetis and colleagues related field potential recordings to simultaneously-measured BOLD data by using the cross-correlation function to determine the impulse response functional relating the two [6]. More recently, Bentley et al., showed that this response function is spatially-variant and frequency dependent [9]. A system that enables concurrent imaging of temporally distinct contrasts provides the means to estimate the response functions that relate these contrasts.

5.2 Final Thoughts

The approaches and findings detailed in this dissertation are meaningful not only for their implications regarding synchronicity and coherence in spontaneous calcium activity but also for their potential as infrastructure for future, more impactful neurophysiological studies. Using fluorophores driven by transgenic expression (GCaMP6) with endogenous contrasts (hemodynamics) provide a chronic imaging capability with invasiveness limited to the initial, one-time optical window implantation. More powerful is the insight gained by using distinct, complementary contrasts that can provide data driven by specific cell populations, vasculature, or individual biochemical processes (e.g. the tricarboxylic acid cycle). This dissertation serves as a starting point for downstream functional imaging studies that will be able to tackle foundational questions unanswered by contemporary neuroscience.

REFERENCES

1. Fox MD, Raichle ME. Spontaneous fluctuations in brain activity observed with functional magnetic resonance imaging. Nat Rev Neurosci. 2007;8(9):700-11. doi: 10.1038/nrn2201. PubMed PMID: 17704812.

2. White BR, Bauer AQ, Snyder AZ, Schlaggar BL, Lee JM, Culver JP. Imaging of functional connectivity in the mouse brain. PloS one. 2011;6(1):e16322. Epub 2011/02/02. doi: 10.1371/journal.pone.0016322. PubMed PMID: 21283729; PubMed Central PMCID: PMC3024435.

3. Bauer AQ, Kraft AW, Wright PW, Snyder AZ, Lee JM, Culver JP. Optical imaging of disrupted functional connectivity following ischemic stroke in mice. NeuroImage. 2014;99:388-401. doi: 10.1016/j.neuroimage.2014.05.051. PubMed PMID: 24862071; PubMed Central PMCID: PMC4332714.

4. Bero AW, Bauer AQ, Stewart FR, White BR, Cirrito JR, Raichle ME, et al. Bidirectional Relationship between Functional Connectivity and Amyloid- Deposition in Mouse Brain. Journal of Neuroscience. 2012;32(13):4334-40. doi: 10.1523/jneurosci.5845-11.2012.

5. Liao F, Hori Y, Hudry E, Bauer AQ, Jiang H, Mahan TE, et al. Anti-ApoE antibody given after plaque onset decreases Abeta accumulation and improves brain function in a mouse model of Abeta amyloidosis. The Journal of neuroscience : the official journal of the Society for Neuroscience. 2014;34(21):7281-92. doi: 10.1523/JNEUROSCI.0646-14.2014. PubMed PMID: 24849360; PubMed Central PMCID: PMCPMC4028501.

6. Logothetis NK, Pauls J, Augath M, Trinath T, Oeltermann A. Neurophysiological investigation of the basis of the fMRI signal. Nature. 2001;412(6843):150-7. doi: 10.1038/35084005. PubMed PMID: 11449264.

7. Vazquez AL, Murphy MC, Kim SG. Neuronal and physiological correlation to hemodynamic resting-state fluctuations in health and disease. Brain connectivity. 2014;4(9):727-40. doi: 10.1089/brain.2014.0276. PubMed PMID: 25300278; PubMed Central PMCID: PMC4238243.

8. Du C, Volkow ND, Koretsky AP, Pan Y. Low-frequency calcium oscillations accompany deoxyhemoglobin oscillations in rat somatosensory cortex. Proceedings of the National Academy of Sciences of the United States of America. 2014;111(43):E4677-86. doi: 10.1073/pnas.1410800111. PubMed PMID: 25313035; PubMed Central PMCID: PMC4217406.

9. Bentley WJ, Li JM, Snyder AZ, Raichle ME, Snyder LH. Oxygen Level and LFP in Task-Positive and Task-Negative Areas: Bridging BOLD fMRI and Electrophysiology. Cerebral cortex. 2016;26(1):346-57. doi: 10.1093/cercor/bhu260. PubMed PMID: 25385710; PubMed Central PMCID: PMCPMC4677981.

10. Devor A, Tian P, Nishimura N, Teng IC, Hillman EM, Narayanan SN, et al. Suppressed neuronal activity and concurrent arteriolar vasoconstriction may explain negative blood oxygenation level-dependent signal. The Journal of neuroscience : the official journal of the Society for Neuroscience. 2007;27(16):4452-9. doi: 10.1523/JNEUROSCI.0134-07.2007. PubMed PMID: 17442830; PubMed Central PMCID: PMCPMC2680207.

11. Liao LD, Tsytsarev V, Delgado-Martinez I, Li ML, Erzurumlu R, Vipin A, et al. Neurovascular coupling: in vivo optical techniques for functional brain imaging. Biomed Eng Online. 2013;12:38. doi: 10.1186/1475-925X-12-38. PubMed PMID: 23631798; PubMed Central PMCID: PMCPMC3655834.

12. Biswal B, Yetkin FZ, Haughton VM, Hyde JS. Functional connectivity in the motor cortex of resting human brain using echo-planar MRI. Magnetic resonance in medicine : official journal of the Society of Magnetic Resonance in Medicine / Society of Magnetic Resonance in Medicine. 1995;34(4):537-41. PubMed PMID: 8524021.

13. Ogawa S, Lee TM, Kay AR, Tank DW. Brain magnetic resonance imaging with contrast dependent on blood oxygenation. Proceedings of the National Academy of Sciences of the United States of America. 1990;87(24):9868-72. PubMed PMID: 2124706; PubMed Central PMCID: PMC55275.

14. Fox PT, Raichle ME. Focal physiological uncoupling of cerebral blood flow and oxidative metabolism during somatosensory stimulation in human subjects. Proceedings of the National Academy of Sciences of the United States of America. 1986;83(4):1140-4. PubMed PMID: 3485282; PubMed Central PMCID: PMC323027.

15. White BR, Culver JP. Phase-encoded retinotopy as an evaluation of diffuse optical neuroimaging. NeuroImage. 2010;49(1):568-77. doi: 10.1016/j.neuroimage.2009.07.023. PubMed PMID: 19631755; PubMed Central PMCID: PMCPMC2785436.

16. White BR, Culver JP. Quantitative evaluation of high-density diffuse optical tomography: in vivo resolution and mapping performance. J Biomed Opt. 2010;15(2):026006. doi: 10.1117/1.3368999. PubMed PMID: 20459251; PubMed Central PMCID: PMCPMC2874047.

17. Eggebrecht AT, White BR, Ferradal SL, Chen C, Zhan Y, Snyder AZ, et al. A quantitative spatial comparison of high-density diffuse optical tomography and fMRI cortical mapping. NeuroImage. 2012;61(4):1120-8. doi: 10.1016/j.neuroimage.2012.01.124. PubMed PMID: 22330315; PubMed Central PMCID: PMCPMC3581336.

18. Ferradal SL, Liao SM, Eggebrecht AT, Shimony JS, Inder TE, Culver JP, et al. Functional Imaging of the Developing Brain at the Bedside Using Diffuse Optical Tomography. Cerebral cortex. 2016;26(4):1558-68. doi: 10.1093/cercor/bhu320. PubMed PMID: 25595183; PubMed Central PMCID: PMCPMC4785947.

19. Eggebrecht AT, Ferradal SL, Robichaux-Viehoever A, Hassanpour MS, Dehghani H, Snyder AZ, et al. Mapping distributed brain function and networks with diffuse optical

tomography. Nat Photonics. 2014;8(6):448-54. doi: 10.1038/nphoton.2014.107. PubMed PMID: 25083161; PubMed Central PMCID: PMCPMC4114252.

20. Grinvald A, Lieke E, Frostig RD, Gilbert CD, Wiesel TN. Functional architecture of cortex revealed by optical imaging of intrinsic signals. Nature. 1986;324(6095):361-4. Epub 1986/11/03. doi: 10.1038/324361a0. PubMed PMID: 3785405.

21. Bergonzi KM, Bauer AQ, Wright PW, Culver JP. Mapping functional connectivity using cerebral blood flow in the mouse brain. Journal of cerebral blood flow and metabolism : official journal of the International Society of Cerebral Blood Flow and Metabolism. 2015;35(3):367-70. doi: 10.1038/jcbfm.2014.211. PubMed PMID: 25492111; PubMed Central PMCID: PMCPMC4348380.

22. Mohajerani MH, McVea DA, Fingas M, Murphy TH. Mirrored bilateral slow-wave cortical activity within local circuits revealed by fast bihemispheric voltage-sensitive dye imaging in anesthetized and awake mice. The Journal of neuroscience : the official journal of the Society for Neuroscience. 2010;30(10):3745-51. doi: 10.1523/JNEUROSCI.6437-09.2010. PubMed PMID: 20220008.

23. Grinvald A, Hildesheim R. VSDI: a new era in functional imaging of cortical dynamics. Nat Rev Neurosci. 2004;5(11):874-85. doi: 10.1038/nrn1536. PubMed PMID: 15496865.

24. Mohajerani MH, Chan AW, Mohsenvand M, LeDue J, Liu R, McVea DA, et al. Spontaneous cortical activity alternates between motifs defined by regional axonal projections. Nature neuroscience. 2013;16(10):1426-35. PubMed PMID: Medline:23974708.

25. Mutoh H, Mishina Y, Gallero-Salas Y, Knopfel T. Comparative performance of a genetically-encoded voltage indicator and a blue voltage sensitive dye for large scale cortical voltage imaging. Front Cell Neurosci. 2015;9:147. doi: 10.3389/fncel.2015.00147. PubMed PMID: 25964738; PubMed Central PMCID: PMCPMC4408844.

26. Xie Y, Chan AW, McGirr A, Xue S, Xiao D, Zeng H, et al. Resolution of High-Frequency Mesoscale Intracortical Maps Using the Genetically Encoded Glutamate Sensor iGluSnFR. The Journal of neuroscience : the official journal of the Society for Neuroscience. 2016;36(4):1261-72. doi: 10.1523/JNEUROSCI.2744-15.2016. PubMed PMID: 26818514.

27. Parsons MP, Vanni MP, Woodard CL, Kang R, Murphy TH, Raymond LA. Real-time imaging of glutamate clearance reveals normal striatal uptake in Huntington disease mouse models. Nature communications. 2016;7:11251. doi: 10.1038/ncomms11251. PubMed PMID: 27052848; PubMed Central PMCID: PMCPMC4829692.

28. Vanzetta I, Grinvald A. Coupling between neuronal activity and microcirculation: implications for functional brain imaging. HFSP journal. 2008;2(2):79-98. doi: 10.2976/1.2889618. PubMed PMID: 19404475; PubMed Central PMCID: PMC2645573.

29. Chance B, Schoener B, Oshino R, Itshak F, Nakase Y. Oxidation-reduction ratio studies of mitochondria in freeze-trapped samples. NADH and flavoprotein fluorescence signals. The Journal of biological chemistry. 1979;254(11):4764-71. PubMed PMID: 220260.

30. Benson RC, Meyer RA, Zaruba ME, McKhann GM. Cellular autofluorescence--is it due to flavins? Journal of Histochemistry & Cytochemistry. 1979;27(1):44-8. doi: 10.1177/27.1.438504.

31. Reinert KC, Gao W, Chen G, Ebner TJ. Flavoprotein autofluorescence imaging in the cerebellar cortex in vivo. Journal of neuroscience research. 2007;85(15):3221-32. Epub 2007/05/24. doi: 10.1002/jnr.21348. PubMed PMID: 17520745.

32. Shibuki K, Hishida R, Tohmi M, Takahashi K, Kitaura H, Kubota Y. Flavoprotein Fluorescence Imaging of Experience-Dependent Cortical Plasticity in Rodents. In: Frostig RD, editor. In Vivo Optical Imaging of Brain Function. Frontiers in Neuroscience. 2nd ed. Boca Raton (FL)2009.

33. Vazquez AL, Fukuda M, Kim SG. Evolution of the dynamic changes in functional cerebral oxidative metabolism from tissue mitochondria to blood oxygen. Journal of cerebral blood flow and metabolism : official journal of the International Society of Cerebral Blood Flow and Metabolism. 2012. Epub 2012/02/02. doi: 10.1038/jcbfm.2011.198. PubMed PMID: 22293987.

34. Shibuki K, Hishida R, Murakami H, Kudoh M, Kawaguchi T, Watanabe M, et al. Dynamic imaging of somatosensory cortical activity in the rat visualized by flavoprotein autofluorescence. J Physiol. 2003;549(Pt 3):919-27. doi: 10.1113/jphysiol.2003.040709. PubMed PMID: 12730344; PubMed Central PMCID: PMCPMC2342977.

35. Reinert KC, Dunbar RL, Gao W, Chen G, Ebner TJ. Flavoprotein autofluorescence imaging of neuronal activation in the cerebellar cortex in vivo. Journal of neurophysiology. 2004;92(1):199-211. Epub 2004/02/27. doi: 10.1152/jn.01275.2003. PubMed PMID: 14985415.

36. Weber B, Burger C, Wyss MT, von Schulthess GK, Scheffold F, Buck A. Optical imaging of the spatiotemporal dynamics of cerebral blood flow and oxidative metabolism in the rat barrel cortex. The European journal of neuroscience. 2004;20(10):2664-70. doi: 10.1111/j.1460-9568.2004.03735.x. PubMed PMID: 15548209.

37. Tohmi M, Kitaura H, Komagata S, Kudoh M, Shibuki K. Enduring critical period plasticity visualized by transcranial flavoprotein imaging in mouse primary visual cortex. The Journal of neuroscience : the official journal of the Society for Neuroscience. 2006;26(45):11775-85. Epub 2006/11/10. doi: 10.1523/JNEUROSCI.1643-06.2006. PubMed PMID: 17093098.

38. Tohmi M, Takahashi K, Kubota Y, Hishida R, Shibuki K. Transcranial flavoprotein fluorescence imaging of mouse cortical activity and plasticity. J Neurochem. 2009;109 Suppl 1:3-9. doi: 10.1111/j.1471-4159.2009.05926.x. PubMed PMID: 19393002.

39. Husson TR, Mallik AK, Zhang JX, Issa NP. Functional imaging of primary visual cortex using flavoprotein autofluorescence. The Journal of neuroscience : the official journal of the Society for Neuroscience. 2007;27(32):8665-75. doi: 10.1523/JNEUROSCI.2156-07.2007. PubMed PMID: 17687044.

40. Kubota Y, Kamatani D, Tsukano H, Ohshima S, Takahashi K, Hishida R, et al. Transcranial photo-inactivation of neural activities in the mouse auditory cortex. Neuroscience research. 2008;60(4):422-30. Epub 2008/02/23. doi: 10.1016/j.neures.2007.12.013. PubMed PMID: 18291543.

41. Sirotin YB, Das A. Spatial Relationship between Flavoprotein Fluorescence and the Hemodynamic Response in the Primary Visual Cortex of Alert Macaque Monkeys. Front Neuroenergetics. 2010;2:6. Epub 2010/06/26. doi: 10.3389/fnene.2010.00006. PubMed PMID: 20577638; PubMed Central PMCID: PMC2890124.

42. Zhao M, Nguyen J, Ma H, Nishimura N, Schaffer CB, Schwartz TH. Preictal and ictal neurovascular and metabolic coupling surrounding a seizure focus. The Journal of neuroscience : the official journal of the Society for Neuroscience. 2011;31(37):13292-300. doi: 10.1523/JNEUROSCI.2597-11.2011. PubMed PMID: 21917812; PubMed Central PMCID: PMC3191875.

43. Yamashita H, Chen S, Komagata S, Hishida R, Iwasato T, Itohara S, et al. Restoration of contralateral representation in the mouse somatosensory cortex after crossing nerve transfer. PloS one. 2012;7(4):e35676. doi: 10.1371/journal.pone.0035676. PubMed PMID: 22536423; PubMed Central PMCID: PMC3334974.

44. Baker WB, Sun Z, Hiraki T, Putt ME, Durduran T, Reivich M, et al. Neurovascular coupling varies with level of global cerebral ischemia in a rat model. Journal of cerebral blood flow and metabolism : official journal of the International Society of Cerebral Blood Flow and Metabolism. 2013;33(1):97-105. doi: 10.1038/jcbfm.2012.137. PubMed PMID: 23032485.

45. Skala M, Ramanujam N. Multiphoton redox ratio imaging for metabolic monitoring in vivo. Methods Mol Biol. 2010;594:155-62. Epub 2010/01/15. doi: 10.1007/978-1-60761-411-1_11. PubMed PMID: 20072916; PubMed Central PMCID: PMC2874879.

46. Li LZ, Xu HN, Ranji M, Nioka S, Chance B. Mitochondrial Redox Imaging for Cancer Diagnostic and Therapeutic Studies. J Innov Opt Health Sci. 2009;2(4):325-41. doi: 10.1142/S1793545809000735. PubMed PMID: 26015810; PubMed Central PMCID: PMCPMC4442014.

47. Grienberger C, Konnerth A. Imaging calcium in neurons. Neuron. 2012;73(5):862-85. doi: 10.1016/j.neuron.2012.02.011. PubMed PMID: 22405199.

48. Tian L, Hires SA, Mao T, Huber D, Chiappe ME, Chalasani SH, et al. Imaging neural activity in worms, flies and mice with improved GCaMP calcium indicators. Nature methods. 2009;6(12):875-81. doi: 10.1038/nmeth.1398. PubMed PMID: 19898485; PubMed Central PMCID: PMCPMC2858873.

49. Zariwala HA, Borghuis BG, Hoogland TM, Madisen L, Tian L, De Zeeuw CI, et al. A Cre-dependent GCaMP3 reporter mouse for neuronal imaging in vivo. The Journal of neuroscience : the official journal of the Society for Neuroscience. 2012;32(9):3131-41. doi: 10.1523/JNEUROSCI.4469-11.2012. PubMed PMID: 22378886; PubMed Central PMCID: PMC3315707.

50. Vanni MP, Murphy TH. Mesoscale transcranial spontaneous activity mapping in GCaMP3 transgenic mice reveals extensive reciprocal connections between areas of somatomotor cortex. The Journal of neuroscience : the official journal of the Society for Neuroscience. 2014;34(48):15931-46. doi: 10.1523/JNEUROSCI.1818-14.2014. PubMed PMID: 25429135.

51. Silasi G, Xiao D, Vanni MP, Chen AC, Murphy TH. Intact skull chronic windows for mesoscopic wide-field imaging in awake mice. J Neurosci Methods. 2016;267:141-9. doi: 10.1016/j.jneumeth.2016.04.012. PubMed PMID: 27102043.

52. Dana H, Chen TW, Hu A, Shields BC, Guo C, Looger LL, et al. Thy1-GCaMP6 transgenic mice for neuronal population imaging in vivo. PloS one. 2014;9(9):e108697. doi: 10.1371/journal.pone.0108697. PubMed PMID: 25250714; PubMed Central PMCID: PMC4177405.

53. Scott BB, Brody CD, Tank DW. Cellular resolution functional imaging in behaving rats using voluntary head restraint. Neuron. 2013;80(2):371-84. doi: 10.1016/j.neuron.2013.08.002. PubMed PMID: 24055015; PubMed Central PMCID: PMC4068252.

54. Heider B, Nathanson JL, Isacoff EY, Callaway EM, Siegel RM. Two-photon imaging of calcium in virally transfected striate cortical neurons of behaving monkey. PloS one. 2010;5(11):e13829. doi: 10.1371/journal.pone.0013829. PubMed PMID: 21079806; PubMed Central PMCID: PMCPMC2973959.

55. Chen TW, Wardill TJ, Sun Y, Pulver SR, Renninger SL, Baohan A, et al. Ultrasensitive fluorescent proteins for imaging neuronal activity. Nature. 2013;499(7458):295-300. doi: 10.1038/nature12354. PubMed PMID: 23868258; PubMed Central PMCID: PMC3777791.

56. Lecrux C, Hamel E. The neurovascular unit in brain function and disease. Acta physiologica. 2011;203(1):47-59. doi: 10.1111/j.1748-1716.2011.02256.x. PubMed PMID: 21272266.

57. Mogi M, Horiuchi M. Neurovascular coupling in cognitive impairment associated with diabetes mellitus. Circulation journal : official journal of the Japanese Circulation Society. 2011;75(5):1042-8. PubMed PMID: 21441696.

58. Iadecola C. Neurovascular regulation in the normal brain and in Alzheimer's disease. Nat Rev Neurosci. 2004;5(5):347-60. doi: 10.1038/nrn1387. PubMed PMID: 15100718.

59. Blicher JU, Stagg CJ, O'Shea J, Ostergaard L, MacIntosh BJ, Johansen-Berg H, et al. Visualization of altered neurovascular coupling in chronic stroke patients using multimodal functional MRI. Journal of cerebral blood flow and metabolism : official journal of the International Society of Cerebral Blood Flow and Metabolism. 2012;32(11):2044-54. doi: 10.1038/jcbfm.2012.105. PubMed PMID: 22828998; PubMed Central PMCID: PMC3493993.

60. Amzica F, Steriade M. Electrophysiological correlates of sleep delta waves. Electroencephalogr Clin Neurophysiol. 1998;107(2):69-83. PubMed PMID: 9751278.

61. Steriade M, Nunez A, Amzica F. A novel slow (< 1 Hz) oscillation of neocortical neurons in vivo: depolarizing and hyperpolarizing components. The Journal of neuroscience : the official journal of the Society for Neuroscience. 1993;13(8):3252-65. PubMed PMID: 8340806.

62. Chauvette S, Crochet S, Volgushev M, Timofeev I. Properties of slow oscillation during slow-wave sleep and anesthesia in cats. The Journal of neuroscience : the official journal of the Society for Neuroscience. 2011;31(42):14998-5008. doi: 10.1523/JNEUROSCI.2339-11.2011. PubMed PMID: 22016533; PubMed Central PMCID: PMC3209581.

63. Walter WG. The location of cerebral tumours by electro-encephalography. Lancet. 1936;2:305-8. PubMed PMID: WOS:000188727900100.

64. Lewis LD, Weiner VS, Mukamel EA, Donoghue JA, Eskandar EN, Madsen JR, et al. Rapid fragmentation of neuronal networks at the onset of propofol-induced unconsciousness. Proceedings of the National Academy of Sciences of the United States of America. 2012;109(49):E3377-86. doi: 10.1073/pnas.1210907109. PubMed PMID: 23129622; PubMed Central PMCID: PMC3523833.

65. Rechtschaffen A. Current perspectives on the function of sleep. Perspect Biol Med. 1998;41(3):359-90. PubMed PMID: 9604368.

66. Fulda S, Romanowski CP, Becker A, Wetter TC, Kimura M, Fenzel T. Rapid eye movements during sleep in mice: high trait-like stability qualifies rapid eye movement density for characterization of phenotypic variation in sleep patterns of rodents. BMC neuroscience. 2011;12:110. doi: 10.1186/1471-2202-12-110. PubMed PMID: 22047102; PubMed Central PMCID: PMCPMC3228710.

67. Massimini M, Huber R, Ferrarelli F, Hill S, Tononi G. The sleep slow oscillation as a traveling wave. The Journal of neuroscience : the official journal of the Society for Neuroscience. 2004;24(31):6862-70. doi: 10.1523/JNEUROSCI.1318-04.2004. PubMed PMID: 15295020.

68. Mitra A, Snyder AZ, Tagliazucchi E, Laufs H, Raichle ME. Propagated infra-slow intrinsic brain activity reorganizes across wake and slow wave sleep. Elife. 2015;4. doi: 10.7554/eLife.10781. PubMed PMID: 26551562; PubMed Central PMCID: PMCPMC4737658.

69. Chen Q, Cichon J, Wang W, Qiu L, Lee SJ, Campbell NR, et al. Imaging neural activity using Thy1-GCaMP transgenic mice. Neuron. 2012;76(2):297-308. doi: 10.1016/j.neuron.2012.07.011. PubMed PMID: 23083733.

70. Hillman EM. Coupling mechanism and significance of the BOLD signal: a status report. Annu Rev Neurosci. 2014;37:161-81. doi: 10.1146/annurev-neuro-071013-014111. PubMed PMID: 25032494; PubMed Central PMCID: PMCPMC4147398.

71. Dunn AK, Devor A, Dale AM, Boas DA. Spatial extent of oxygen metabolism and hemodynamic changes during functional activation of the rat somatosensory cortex. NeuroImage. 2005;27(2):279-90. doi: 10.1016/j.neuroimage.2005.04.024. PubMed PMID: 15925522.

72. Lauritzen M. Reading vascular changes in brain imaging: is dendritic calcium the key? Nat Rev Neurosci. 2005;6(1):77-85. doi: 10.1038/nrn1589. PubMed PMID: 15611729.

73. Laumann TO, Gordon EM, Adeyemo B, Snyder AZ, Joo SJ, Chen MY, et al. Functional System and Areal Organization of a Highly Sampled Individual Human Brain. Neuron. 2015;87(3):657-70. doi: 10.1016/j.neuron.2015.06.037. PubMed PMID: 26212711; PubMed Central PMCID: PMCPMC4642864.

74. Laumann TO, Snyder AZ, Mitra A, Gordon EM, Gratton C, Adeyemo B, et al. On the Stability of BOLD fMRI Correlations. Cerebral cortex. 2016. doi: 10.1093/cercor/bhw265. PubMed PMID: 27591147.

75. Liu X, Yanagawa T, Leopold DA, Fujii N, Duyn JH. Robust Long-Range Coordination of Spontaneous Neural Activity in Waking, Sleep and Anesthesia. Cerebral cortex. 2015;25(9):2929-38. doi: 10.1093/cercor/bhu089. PubMed PMID: 24812083; PubMed Central PMCID: PMCPMC4537437.

76. Stroh A, Adelsberger H, Groh A, Ruhlmann C, Fischer S, Schierloh A, et al. Making waves: initiation and propagation of corticothalamic Ca2+ waves in vivo. Neuron. 2013;77(6):1136-50. doi: 10.1016/j.neuron.2013.01.031. PubMed PMID: 23522048.

77. Tononi G, Cirelli C. Sleep and the price of plasticity: from synaptic and cellular homeostasis to memory consolidation and integration. Neuron. 2014;81(1):12-34. doi: 10.1016/j.neuron.2013.12.025. PubMed PMID: 24411729; PubMed Central PMCID: PMCPMC3921176.

78. Mitra A, Snyder AZ, Blazey T, Raichle ME. Lag threads organize the brain's intrinsic activity. Proceedings of the National Academy of Sciences of the United States of America. 2015;112(17):E2235-44. doi: 10.1073/pnas.1503960112. PubMed PMID: 25825720; PubMed Central PMCID: PMC4418865.

79. Matsui T, Murakami T, Ohki K. Transient neuronal coactivations embedded in globally propagating waves underlie resting-state functional connectivity. Proceedings of the National Academy of Sciences of the United States of America. 2016;113(23):6556-61. doi: 10.1073/pnas.1521299113. PubMed PMID: 27185944.

80. Kozberg MG, Ma Y, Shaik MA, Kim SH, Hillman EM. Rapid Postnatal Expansion of Neural Networks Occurs in an Environment of Altered Neurovascular and Neurometabolic Coupling. The Journal of neuroscience : the official journal of the Society for Neuroscience. 2016;36(25):6704-17. doi: 10.1523/JNEUROSCI.2363-15.2016. PubMed PMID: 27335402.

81. Hull E, Ediger M, Unione A, Deemer E, Stroman M, Baynes J. Noninvasive, optical detection of diabetes: model studies with porcine skin. Opt Express. 2004;12(19):4496-510. PubMed PMID: 19484001.

82. Marinkovic P, Godinho L, Misgeld T. Generation and Screening of Transgenic Mice with Neuronal Labeling Controlled by Thy1 Regulatory Elements. Cold Spring Harb Protoc. 2015;2015(10):875-82. doi: 10.1101/pdb.top087668. PubMed PMID: 26430261.

83. Girouard H, Iadecola C. Neurovascular coupling in the normal brain and in hypertension, stroke, and Alzheimer disease. J Appl Physiol (1985). 2006;100(1):328-35. doi: 10.1152/japplphysiol.00966.2005. PubMed PMID: 16357086.

84. Brier MR, Thomas JB, Snyder AZ, Benzinger TL, Zhang D, Raichle ME, et al. Loss of intranetwork and internetwork resting state functional connections with Alzheimer's disease progression. The Journal of neuroscience : the official journal of the Society for Neuroscience. 2012;32(26):8890-9. doi: 10.1523/JNEUROSCI.5698-11.2012. PubMed PMID: 22745490; PubMed Central PMCID: PMCPMC3458508.

85. Busche MA, Kekus M, Adelsberger H, Noda T, Forstl H, Nelken I, et al. Rescue of long-range circuit dysfunction in Alzheimer's disease models. Nature neuroscience. 2015;18(11):1623-30. doi: 10.1038/nn.4137. PubMed PMID: 26457554.

86. Karmarkar SW, Bottum KM, Tischkau SA. Considerations for the use of anesthetics in neurotoxicity studies. Comp Med. 2010;60(4):256-62. PubMed PMID: 20819374; PubMed Central PMCID: PMCPMC2930323.

87. Tsukamoto A, Serizawa K, Sato R, Yamazaki J, Inomata T. Vital signs monitoring during injectable and inhalant anesthesia in mice. Exp Anim. 2015;64(1):57-64. doi: 10.1538/expanim.14-0050. PubMed PMID: 25312399; PubMed Central PMCID: PMCPMC4329516.

88. Tabuchi S, Tsunematsu T, Black SW, Tominaga M, Maruyama M, Takagi K, et al. Conditional ablation of orexin/hypocretin neurons: a new mouse model for the study of narcolepsy and orexin system function. The Journal of neuroscience : the official journal of the Society for Neuroscience. 2014;34(19):6495-509. doi: 10.1523/JNEUROSCI.0073-14.2014. PubMed PMID: 24806676; PubMed Central PMCID: PMCPMC4012309.

89. Mitra A, Snyder AZ, Hacker CD, Raichle ME. Lag structure in resting-state fMRI. Journal of neurophysiology. 2014;111(11):2374-91. doi: 10.1152/jn.00804.2013. PubMed PMID: 24598530; PubMed Central PMCID: PMC4097876.

90. Mitra A, Snyder AZ, Constantino JN, Raichle ME. The Lag Structure of Intrinsic Activity is Focally Altered in High Functioning Adults with Autism. Cerebral cortex. 2015. doi: 10.1093/cercor/bhv294. PubMed PMID: 26656726.

91. Dana H, Mohar B, Sun Y, Narayan S, Gordus A, Hasseman JP, et al. Sensitive red protein calcium indicators for imaging neural activity. Elife. 2016;5. doi: 10.7554/eLife.12727. PubMed PMID: 27011354; PubMed Central PMCID: PMCPMC4846379.